5-2022

Thermodynamic Analysis of a Novel Cycle for Nuclear SMR and Heat Transfer Performance Validation of the Related Supercritical Working Fluids

Benjamin M. Pepper
Utah State University

THERMODYNAMIC ANALYSIS OF A NOVEL CYCLE FOR NUCLEAR SMR AND HEAT TRANSFER PERFORMANCE VALIDATION OF THE RELATED SUPERCRITICAL WORKING FLUIDS

by

Benjamin M. Pepper

A thesis submitted in partial fulfillment
of the requirements for the degree

of

MASTER OF SCIENCE

in

Mechanical Engineering

Approved:

Hailei Wang, Ph.D. Major Professor	Nicholas Roberts, Ph.D. Committee Member
Som Dutta, Ph.D. Committee Member	D. Richard Cutler, Ph.D. Interim Vice Provost of Graduate Studies

UTAH STATE UNIVERSITY
Logan, Utah

2022

ABSTRACT

Thermodynamic Analysis of a Novel Cycle for Nuclear SMR and Heat Transfer Performance Validation of the Related Supercritical Working Fluids

by

Benjamin M. Pepper, Master of Science

Utah State University, 2022

Major Professor: Hailei Wang, Ph.D.
Department: Mechanical and Aerospace Engineering

A model for the simulation of a novel regenerative transcritical power cycle for a nuclear small modular reactor (SMR) is constructed based on a fixed range of design parameters and desired system performance. A parametric grid search of independent variables evaluates cycle performance when incorporating different pure and binary mixture working fluids into the design. Performance is evaluated and compared to current design benchmarks. While performance is not enhanced with selected mixtures, pure alcohol coolants achieved desirable performance, motivating a better understanding of thermodynamic and heat transfer characteristics of alcohol-based working fluids. A continuous pumped loop system equipped with a cooling, regenerative, and test section heat exchanger is constructed to experimentally characterize the heat transfer behavior of chosen heat transfer fluids near their critical points. Under fixed temperature boundaries, and with local flux measurements, heat flow is analyzed with mixed flow conditions in a wide aspect ratio rectangular channel. The data are validated via results from similar experiments and correlations. Preparations are made for future analysis of corrosive/reactive fluids under perturbed flow conditions.

(99 pages)

PUBLIC ABSTRACT

Thermodynamic Analysis of a Novel Cycle for Nuclear SMR and Heat Transfer Performance Validation of the Related Supercritical Working Fluids

Benjamin M. Pepper

Currently, all operating nuclear power facilities in the U.S. follow the same general design and process: light-water reactors boil water into steam using bundles of nuclear fuel rods as a heat source, pumping that steam through a turbine which powers a generator to produce clean year-round electricity. Water is an effective coolant, but other facilities around the world have demonstrated the ability to use non-water-based coolants in nuclear reactor designs, which consequently have their own trade-offs. Some positive consequences of using different reactor designs include enhanced safety, better economics, and cheaper clean consumer energy. The work described in this paper begins with a computer model of a nuclear reactor design that uses non-water-based coolants, both pure fluids and mixtures, and measures the performance based on a few metrics. While the model did not show that the selected mixtures worked well as coolants, some of the pure fluids did lead to reactor performance at least as good as the water-based counterpart. This motivated a physical experiment that was built to better document and understand the ability for these pure fluids to transfer heat under specific conditions. These conditions include different fluid phases such as liquid or gas, and even supercritical liquids or gases which exist at higher pressures and temperatures. The boundary between supercritical phases are less clear and the distinction between them are less definite if measured by their physical properties. The experimental setup was validated to accurately capture and measure the desired heat transfer behaviors for selected fluids. The design is also future-proofed by utilizing modularity of components and by fabricating new components for testing corrosive/reactive fluids.

ACKNOWLEDGMENTS

Thanks to my primary investigator, Hailei Wang, for his constant push towards success and kind patience. Thanks to my supporting committee, Som Dutta for his guidance and wisdom, and Nicholas Roberts for the like, and without him I never would have found my place in a research laboratory.

Thanks to Yili Zhang and Jacob Bryan for their prolific skills with scripting and sharing their knowledge in the field. Thanks to Mahdi Ghorbani for his contributions to understanding and performing uncertainty analysis.

Thanks to Ammon Black for helping get work off the ground and Aiden Meek for his significant contributions to design, analysis, and fabrication during a busy schedule.

Big thanks to Derick Botha and the support of NuScale Power, LLC for guiding the computational project included in this thesis. Thank you to the Nuclear Regulatory Commission for its support in the continuing work and experimentation herein.

Lastly, the biggest thanks to my amazing partner, Emily. Without her, I never would have found the courage and drive to continue my education and make it through the difficult stages of the process. You are constantly transforming me into a better person each and every day.

Benjamin M. Pepper

CONTENTS

LIST OF TABLES

LIST OF FIGURES

ACRONYMS

CSP	concentrated solar power
DOF	degree(s) of freedom
EtOH	ethanol
FS	factor of safety
HP	high-pressure
HTF	heat transfer fluid
LCOE	levelized cost of energy
LP	low-pressure
MD	molecular dynamics
MeOH	methanol
NN	neural network
ORC	organic Rankine cycle
s	supercritical (used as prefix to other acronyms)
SMR	small modular reactor
WF	working fluid
WHR	waste heat recovery

SYMBOLS

A_c	cross-sectional area [m^2]
c_p	isobaric specific heat [$kJ \cdot kg^{-1}K^{-1}$]
$\Delta_{vap}H^\circ$	heat of vaporization [$kJ \cdot kg^{-1}$]
ρ	density [$kg \cdot m^{-3}$]
ε	error threshold
η	efficiency
γ	Ratio of specific heats
Gr	Grashof number
λ	thermal conductivity [$W \cdot m^{-1}K^{-1}$]
$\dot{m}$	mass flow rate [$g \cdot s^{-1}$]
μ	dynamic viscosity [$Pa \cdot s$]
ν	kinematic viscosity [$m^2 \cdot s^{-1}$]
Nu	Nusselt Number
P_c	critical pressure [MPa]
Π	pressure ratio (P_{in}/P_{out})
Pr	Prandtl number
q	heat flux [$W \cdot m^{-2}$]
$\dot{Q}$	rate of heat transfer [W]
Re	Reynolds number
R_{eff}	effective thermal resistance [$K \cdot W^{-1}$]
T_c	critical temperature [K]
u	flow velocity [$m \cdot s^{-1}$]
$\dot{V}$	volumetric flow rate [$m^3 \cdot s^{-1}$]
$\dot{W}$	rate of work produced [W]
ξ	percentage of fluid stream split, bounded on [0, 1]

CHAPTER 1

INTRODUCTION

1.1 Motivation of Research

There is a special phenomenon with fluids that exist in the thermodynamic state near their critical pressure and temperature. The well-defined boundaries between the phases of matter a fluid can exist as become less clear here, due to an attenuation of the energy barrier dividing them. By more easily traversing phase boundaries, characteristics of the fluid can shift greatly with minor thermodynamic perturbations. This physically manifests as steep gradients and large peaks in measurable thermophysical properties such as heat capacity, thermal conductivity, density, and viscosity. Because of this, supercritical fluids generally posses desirable heat transfer properties that allow them to serve well as working fluids in power generation systems, heat pumps, and efficient heat sink applications [1, 2]. However, the rapid changes in physical behavior force careful engineering into the raw components design, choice of working fluid, and optimization of cycle parameters within their applications.

The majority of power generation systems utilize water as a coolant because it posses a large latent heat of vaporization, along with the fact that it is cheap and prevalent. However, it is difficult to run a heat transfer process with supercritical water due to the requisite immense pressures. Other compounds, such as organic substances, have been demonstrated as working fluids to operate in useful heat transfer processes without the need of comparatively expensive infrastructure. Prevalence of the organic Rankine cycle (ORC) has increased significantly over the last couple of decades, due to its ability to harvest heat from sources generally left untapped and economic feasibility of well-engineering designs [3–5]. Their use is found in numerous applications such as waste heat recovery (WHR), geothermal energy capture, desalination and other production processes, and in power generation [6, 7]. Fur-

ther improvements to power generation has been demonstrated by trans- or supercritical ORCs (sORC) [8–10] by choosing working fluids that operate in a thermodynamic cycle partially or entirely within the supercritical region. Some of the benefits include higher cycle efficiency, minimized component size, and better temperature matching between fluid streams. This technology has the potential to make cheaper energy more widely accessible, reduce energy losses, improve manufacturing processes, and reduce reliability on fossil fuel energy.

The source of thermal energy is a major factor in determining a suitable working fluid to substitute for water in the power cycle. A working supercritical fluid must operate around a controlled temperature range, preferably pulling heat from a constant power source. Sources such as exhaust and flue gases, geothermal islands, concentrated solar power (CSP), and nuclear fuel rods/pellets behave this way and stand as a proper foundation for designing a reliable ORC generation system. This paper will first focus on a nuclear-fueled cycle of constant power output.

The design of a novel regenerative transcritical methanol power cycle for a nuclear small modular reactor (SMR) has been demonstrated to have desirable performance along with other benefits over common Gen III and some Gen IV nuclear reactor designs. This paper explores the possibility of utilizing a new power cycle design with a binary mixture as a working fluid. This design model is constructed using a prescribed thermodynamic cycle proposed by NuScale Power in order to aid further development of SMR reactors beyond that of their first reactor design approved by the Nuclear Regulatory Commission. Thermodynamic analysis of the system is applied to determine the overall system performance and elucidate pertinent behaviors of each identified working fluid. With proper engineering, this design may help widen the availability of nuclear power to a larger customer pool and pave the way for enhanced processing and approval of new nuclear system and reactor designs.

The goal through this research is to close the gap in reliable data for an energy conversion system using unconventional working fluids. This system specifically focused on an energy conversion process for a small modular nuclear reactor operating within a tempera-

ture range common among light-water reactors above supercritical pressures using new pure compounds and binary mixtures as working fluids. The new proposed design is coupled with the same safety standards as many Gen IV reactor designs to reduce risk of meltdown by maintaining a "walk away" safety standard.

The allowable range that independent variables in the novel reactor design may vary within is quite narrow, such as the maximum pressure or minimum coolant temperature. Therefore, the coolant itself is left as the variable with the most wiggle room, motivating other fluids of interest to be tested. Coupling the simulated results of the power cycle design, this study also experimentally investigates the heat transfer behavior of r134a during controlled heat input near its supercritical point. This refrigerant is chosen since the fluid has been well documented in literature [11] and serves and a groundwork validation. An experimental characterization is desirable since numerical simulations often lose accuracy due to complex flow and heat transfer phenomena near the critical point of a fluid for the prediction of its behavior or properties. The physical analysis aims to isolate the necessary control and specific behaviors of the fluid under prescribed conditions. This will aid in the future design of a system for controlled thermal analysis of fluids operating within or near their supercritical points - also referred to as the pseudocritical region. This can manifest in design and orientation of heat exchangers for supercritical fluids and better collective understanding of those that are poorly characterized.

A generic diagram of the constructed pumped cycle loop apparatus is shown in Fig 1.1 for basic understanding of the experimental setup. Design of the specific apparatus constructed is shown an further discussed in chapter 4. Thorough design considerations and analyses are performed specifically for the test section component, which houses the majority of the sensing equipment for data collection. Two versions of the test section are fabricated for both introductory validation and for analysis of a wide range of fluids. These are discussed further in sections 4.2.1 and 4.2.2 respectively. The results of the experiment document performance of the test sections for reliable data acquisition and analysis along with measurements of heat transfer properties of supercritical fluids. The latter aims to

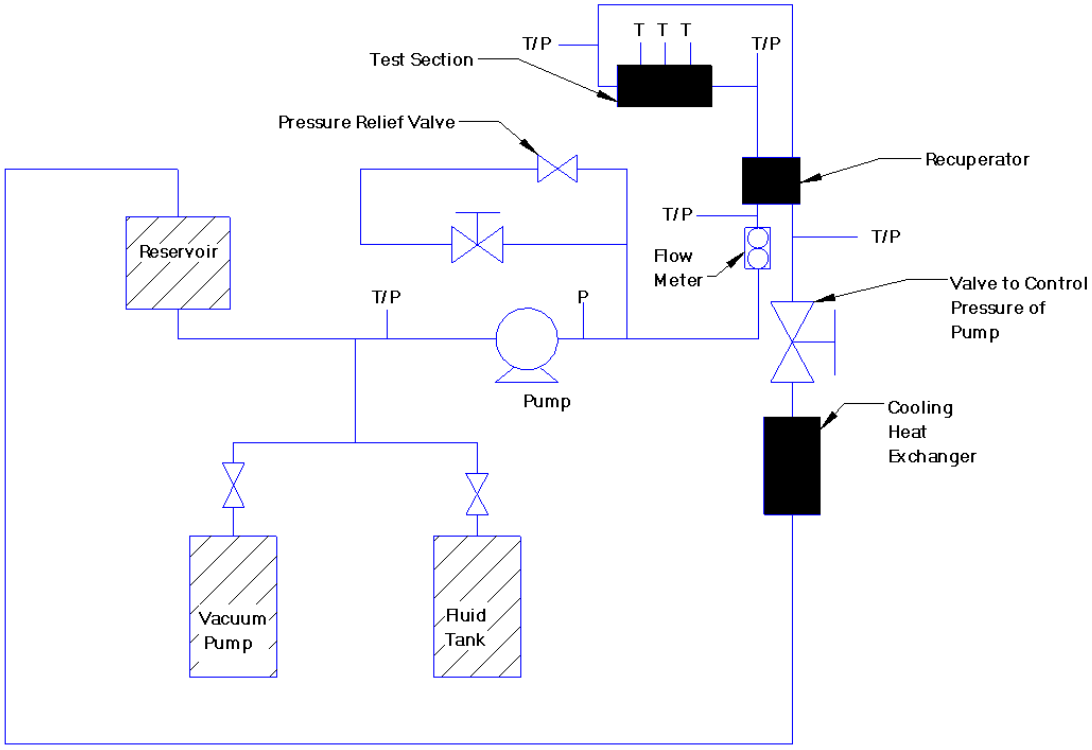

Fig. 1.1: Generic diagram of the experimental apparatus

validate theoretical fluid calculations and heat transfer correlations for related supercritical fluids. This will enhance baseline engineering design for power generating and hybrid energy ORCs utilizing similar fluids while laying the groundwork for the investigation of other fluids of interest.

1.2 Overview of Projects

A model for the performance of a novel regenerative mixed-fluid transcritical cycle is constructed using the `MATLAB` and `Python` language compilers and fluid data from the `CoolProp` [12] library. The performance is quantified using thermodynamic equations to define the state of the fluid at specific points in the system and determine the power extracted through the expanders and output by the generator. The pertinent independent variables specified are the parameters of the working fluid (specific compound, pure or mixed, etc.), the floor and ceiling of the system pressure range, and percentage of working fluid mass flow diverted or power output used for recuperative processes in the system (parasitic losses).

In addition to net power out, other system-level dependent variables are quantified such as first-law efficiency, mass-flow rates of the coolant, and a penalty term used to quantify violations in thermodynamic and system processes.

Supplementing this nuclear system model, an experimental apparatus for the controlled analysis of a heated supercritical fluid is built to better understand heat transfer behaviors and characteristics under steady flow conditions. Consideration is made for both commonly used heat transfer fluids and other fluids of interest for this research. Characterization of heat transfer behaviors of supercritical R134a is measured for the fluid flowing through a wide aspect ratio rectangular channel included in a continuous pumped loop apparatus. Heat transfer into the fluid is monitored while a constant temperature boundary is maintained at the edge of the heating components in the test section. This data is used to validate the working design of the system and aid in the development of additional robust test sections for highly corrosive or reactive fluids for future characterization tests.

Determining the fundamental behaviors of organic fluids around their respective critical points will benefit any future studies and optimizations focusing on supercritical energy conversion systems. The pertinent goal of an experimental study with lower critical parameters, such as methanol, is to fundamentally characterize and determine the optimal operating constraints. Therefore, one can maximize thermal energy absorption by the fluid, ergo maximizing the ability to siphon thermal energy from low and mid grade heat sources and convert the energy to useful work. It is also beneficial to understand the high level of control necessary to operate fluids in a cycle where thermodynamic states are transient from a physical, operational, and safety point of view.

With these coupled simulations and experiments, extracting heat from mid-grade temperature sources can be made more efficient and economically viable due to enhanced engineering design and understanding. With this research, the option to utilize new working fluids for thermodynamic cycles unlocks new possibilities for ORC technology, and both powered and passive thermal systems.

1.3 Overview of Topics

The remainder of this document is divided into the following chapters:

- Chapter II. Literature Review: A review of current work in the literature relevant to supercritical fluids and power cycles utilizing their benefits is discussed.
- Chapter III. A Novel Power Cycle for Nuclear SMR: The computational simulation project is introduced along with the methodology behind the model. Following are the results and discussion of the parameters and performance data.
- Chapter IV. Experimental Heat Transfer Performance Validation: The experimental validation project is introduced along with the methods, equations, and assumptions used. Included thereafter are the results and related uncertainty analysis.
- Chapter V. Conclusions: The overall process and results for each project with their respective findings culminate in a succinct summary.

Immediately following these chapters in order are itemized references and additional appendices.

CHAPTER 2
LITERATURE REVIEW

2.1 The Organic Rankine Cycle

The concept of the ORC has existed for over a century with the principle technology being established as early as 1825 when Thomas Howard experimented with ether (alcohols) as an engine working fluid [13]. This was well before the publishing of William Rankine's famous manual on engine design 34 years later. The ORC system follows the same principles as a traditional Rankine cycle, but substitutes an organic compound as the working fluid in lieu of water. Since the development of a stable power system by Bronicki and Tabor in the early 1960s and soaring energy prices in the 70s, ORC technology has been implemented into many industrial and commercial processes. Organic working fluids are selected based on power plant design and the available heat source, but truly shine in systems designed for a capacity on the order of megawatts with nominal heat source temperatures less than 400°C [7, 14]. Possible benefits of ORC systems include utilizing more efficient turbomachinery and other components, reducing the low-pressure vacuum at the condenser, and favorable performance to other gas cycles for an optimized application [15]. Many common working fluids, such as refrigerants and inert gases like carbon dioxide, can be utilized for an ORC [16, 17]. In addition to these perks, the wide range of organic heat transfer fluids and the maturity of the standard Rankine cycle power generation process has garnered unyielding research interest in expanding the capabilities and applications of the ORC.

Ringler et al. [18] evaluated the feasibility of a WHR Rankine cycle system for an internal combustion (IC) engine. Using the Dymola simulation tool, two systems (exhaust stream and coolant + exhaust) were parametrically analyzed with water and ethanol as the system working fluids respectively. It was determined that the ethanol system's efficiency was generally low (≈10%) but was only a function of the exhaust gas temperature (with

fixed evaporation temperature) and so will continually increase as the exhaust stream gets hotter. The cycle with water saw larger efficiencies (≈19%) but demonstrated a complex relationship with efficiencies capping off regardless of increasing exhaust heat. A subsequent experiment performed power analysis on the two-loop design using an alcohol coolant. This further demonstrated the decaying power recovery with an increase in engine power output (speed), remaining relatively linear until an inflection point around 65 mph. This decay is due to a couple of reasons. Firstly, the internal combustion engine becomes more efficient at higher outputs, making the subsequent WHR process less so. Secondly, the dual-loop system becomes less efficient at removing heat from the system at high loads. This is then the optimal working design for a single-loop, water-based Rankine cycle. However, with average travel speeds generally less than 65 mph, the ethanol-based WHR system proves a viable method for boosting fuel utilization in IC engines. In another approach to an ORC for WHR, a study was performed by Nawi et al. [19] investigating a bioethanol system capturing marine diesel engine exhaust heat. A model of a marine engine system, comprised of a six-cylinder turbocharged diesel engine and a dual-fuel low-temperature IC engine, were designed and the cycle equated through thermodynamic relations of the pump, evaporator, condenser, and turbine. Mass flows were tested for engine loads at four states between 50% to 100% load. The resulting thermal efficiency of the system peaked for the lowest engine load tested at about 2.3% and remained half as high when increased to 100% load. For each test, the efficiency increased linearly with the exhaust gas outlet temperature. Despite low efficiencies, power outputs from these ORC cycles still produced a few kilowatts. Better yet, the use of bioethanol algae as a working fluid provides zero detriment to the environment as it's perfectly clean and readily abundant. However, the issue remains to make this economically feasible, since it's difficult to make a return on the large investment needed for the balance of systems.

As with all products in a free market, risk and economics of design are a constant counterweight on the balance for innovation and environmental benefit. This allocation of financial resources makes development of energy-saving measures difficult, even when

energy recovery systems pose only a benefit to communities and the environment. Ethanol-based WHR systems do not have spectacular efficiencies and require a significant balance of systems. However, ethanol is not very expensive and abundant, and with additional research into utilizing ethanol and similar fluids for these purposes, performance and prices will only become more competitive.

With adaptability to both size and sources, access for ORC power systems is available to a wide range of system implementations, including variable waste heat in complex systems, such as recovery from engine oils, coolant, or flue gases [20, 21]. These systems may also include concentrated solar power (CSP), nuclear power, geothermal, or biomass heat recovery too, due to the steadiness of the thermal island heat source. Most ORC power cycle applications focus on low-temperature applications (below 250°C) due to the decreased economy of ORC systems designed for large capacity [6, 22].

Years of simulation and experimentation have broadened the reach and applications of ORCs and continued to improve economic and working aspects of the technology. The use of light alcohols as the primary cycle working fluid poses numerous benefits in some ORC applications, such as increasing the thermal exchange capacity, improving thermal efficiency via novel fluids and fluid states, and the ability to adapt power systems to a broader range of heat sources. Comparatively, the critical points of methanol and ethanol are similar and lie at mid-level temperature ranges when compared to commonly used organic fluids and water. This optimizes the heat source temperature range for these fluids to be between 250-400°C, ideal for small modular reactors (SMR) [23,24], CSP [25], and WHR systems. Furthermore, these exhaust stream temperatures are very common among gasoline and diesel powered transportation and cargo carrier vessels, both automotive and seafaring. Conservatively, around 50% of the fuel energy content of maritime transportation vessels is dissipated as waste heat [20], and higher for IC engine automobiles and trucks. The use of light alcohols pose a cheap and prevalent source for thermal capture to improve the performance of these systems, therefore reducing thermal waste which pollutes both animal and human habitats. Moreover, sustainable power generation and energy conversion systems are making a move

to the decentralized small-scale in order to meet the demands of communities without the additional cost of infrastructure associated with power transmission and reducing the need for brick-and-mortar establishments. Subsequently, the reduced form factors of power cycle components in these applications make for a strong candidate in decentralized power distribution. For power outputs less than 100[MW], and for a range of plausible heat sources, the ORC system is the most viable solution to meet demand [4].

Around 52% of the global energy production and 72% of primary energy consumption is lost through heat dissipation [4]. Therefore, not just nuclear power system can make use of ORC technology. With the available heat sources for an ORC process being just shy of limitless, the improvement of heat recovery systems is an important step towards net-zero energy production and a healthier planet for future generations.

2.2 Applications of Supercritical Phenomena

Interest has been increasing in higher temperature applications due to manufacturing improvements for components and optimization of trans- and supercritical thermodynamic cycles. The performance benefits of supercritical power cycles over their subcritical counterparts include more favorable thermodynamic characteristics [26] and thermal transport behaviors [27]. A reduction in the size of system components, enhanced thermal performance in heat exchangers, and reduced initial investment costs have all been recorded as benefits from technology exploiting supercritical fluid characteristics [9, 28].

The reduced supercritical and boiling points, and variable thermodynamic properties such as isentropic or negative vapor curves (dry fluids), pose organic working fluids as beneficial over water-based counterparts by simplifying components to handle a single fluid phase [29]. Furthermore, the choice of a working fluid for specific heat source temperatures provides a better means of sensible temperature matching between the working fluid and the heat source. This improves dynamic heat transfer to the coolant and performance may be further engineered for specific applications by using multicomponent working fluids [30, 31].

Lesser studied working fluids such as methanol and ethanol are poised as prime suspects in advancing the application of the ORC in the mid-temperature region (250°C-400°C) and

CO_2 for high temperature system designs [24, 32, 33]. Working fluid selection is guided by characteristics of the fluid that may include its critical and boiling points, latent heat, and how wet/dry the fluid's vapor curve is in this application [6]. A comparison of fluid fluid-vapor domes can be referenced in Fig A.1 along with more properties of selected fluids which can be viewed in Table A.1. These characteristics determine which fluids are best suited for a specific set of system design parameters.

Other experiments analyzing the thermal exchange behaviors of many supercritical organic fluids have demonstrated the situational benefits to different organic fluids, mainly ethanol's performance benefits at mid-range temperatures [34]. Buoyancy-driven cycles for exhaust WHR has also been proposed with heat transfer performance being evaluated using k-ω turbulence models [35]. Since thermo-physical properties of a fluid passing through its supercritical region rapidly change, especially near the supercritical pressure (see Fig A.2), the drastic density fluctuations can drive local fluid motion quite significantly. These buoyancy-driven aspects provide economic advantages by reducing the complexity of some components and has been demonstrated in practice on the industrial scale by companies such as NuScale Power [36]. Academic investigations have developed innovations that have improved power cycle system performance in nuclear power systems, including SMR designs for smaller scale facilities, adapting to mid- and high-temperature sources, and using supercritical cycle designs. However, when working with fluids other than pure, common, or industrially utilized ones, poor theoretical thermodynamic calculations may persist. Theory makes good compensation for this by quantifying parameters such as nonideality or activity coefficients and through models such as Margules activity model or the GERG equation of state [37]. However, physical data produces the best picture for the behavior of a working fluid in operation. Many pure fluids are well characterized via experiment, but the number of possible fluid mixtures far overshadows their number. Emerging simulation technology and more robust computational hardware is slowly closing the gap in calculation time, but convergence values are not always accurate. For working fluids other than pure compounds,

these simulation and optimization applications help to motivate the physical characterization of these uncommon choices of fluids with possible benefits to their applications.

The evaluation of both flow and heat transfer characteristics for refrigerants and alcohol-based working fluids has been performed experimentally in many cases. Determining the useful thermal transport behaviors of a working fluid (i.e. optimizing the Nusselt number in heat exchanger architectures) allows for the enhancement of engineering design for components and systems pertinent to heat transfer. The heat transfer performance of supercritical refrigerants has been experimentally evaluated for certain flow regimes and pipe/channel geometries [28, 38]. The performance of supercritical CO_2 utilized in a high-temperature Brayton cycle has also been experimentally evaluated quite extensively due to the low health and safety risks associated with the working fluid [39, 40]. Effective dual-loop designs have also demonstrated enhanced performance by combining multiple fluids and utilizing buoyancy-driven flows to reduce noise and complexity [41]. A similar experiment combined the benefits of supercritical working fluids with a MeOH heat pipe to develop a low-maintenance geothermal system design suitable for private residences [33].

Regrettably, these efficient energy conversion processes are often restricted to primary heat sources at extreme (below 180°C and over 400°C) temperatures, leaving a critical mid-temperature range generally untapped. This paper is motivated to investigate current trends in the literature concerned with thermophysical performance of organic working fluids in energy conversion systems for application to a light-water nuclear reactor. This will provide a background comparing thermophysical behaviors of common low- and high-temperature fluids by identifying the critical constraints limiting them to specific source temperature regimes. This background, combined with novel simulation and experiment studies, will help make predictions for introducing viable mid-temperature fluids, such as methanol, to preserve the adaptability of organic Rankine cycle systems to a broad range of engineering applications and improving the capabilities of matured light-water reactor systems.

Heavily investigated in the literature, sCO_2 is a desirable working fluid due to its maturity, safety in operation and environment, and optimized potential utilizing the Brayton

cycle. Helium gas has been eyed for similar high temperature designs. However, the system is best suited for superheated temperature systems near 800°C or even higher. Some refrigerants, such as R134a and R22, have been experimentally demonstrated to be effective at low-temperature implementations. Therefore, there remains a critical mid-temperature regime left untapped by a well-optimized and mature working fluid.

CHAPTER 3
A NOVEL POWER CYCLE FOR NUCLEAR SMR

3.1 Project Overview

An investigation into the efficacy of utilizing certain multi-component working fluids for a nuclear SMR is proposed by NuScale Power. The system in question is expected to meet or exceed performance metrics of a baseline cycle model, shown in Fig 3.1 from [42]. This new model is being investigated as an extension of the baseline design in order to draw further conclusions about new working fluids and possible mixtures of interest, which can inform design choices for future systems. Novel coolants have the possibility of achieving acceptable cycle performance while reducing the complexity of the nuclear power system.

A set of two mixtures were specified to be further investigated as potential working fluids in the transcritical cycle. These mixtures include EtOH and MeOH alcohols mixed with carbon dioxide (CO_2) gas. Initially, the desire to simulate alcohol mixtures with carbon monoxide was proposed. However, the possibility of chemical reactions (such as the spontaneous formation of methyl formate) under the thermal conditions of the cycle and the higher complexity of molecular interactions between highly polar compounds could not be ignored. Due to these issues, only carbon dioxide was used as an additive component.

For this cycle design, two components are determinant in the performance of this system: the regenerator and the compressor. The performance in the regenerator determines if the temperature glide of the two-phase mixture provides enhancements to thermal energy exchange. Analysis of the compressor determines if the power required to pressurize the gas in the system outweighs the benefits provided by a mixture working fluid. This compressor analysis is coupled with analysis of solubility behavior between the constituents of the working fluid. The overall performance optimization of the cycle is evaluated via a parametric grid search.

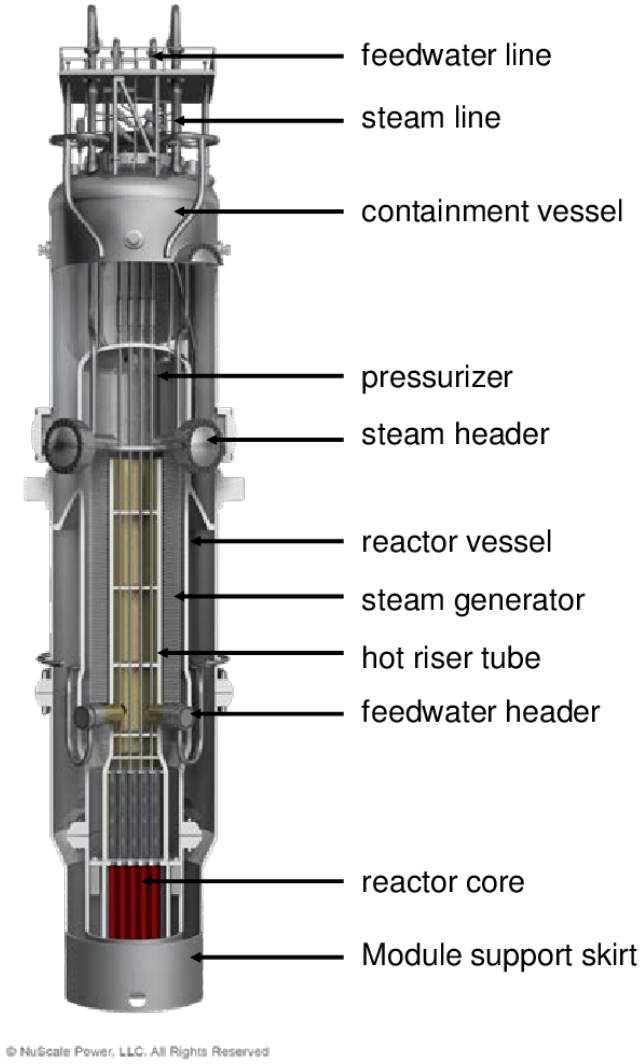

Fig. 3.1: Schematic of the baseline SMR module by NuScale Power

3.1.1 Model Design

The initial prescription from NuScale for the cycle is outlined by the T-s diagram illustrated in Fig 3.2. Each numbered station refers to a specific thermodynamic state of the coolant as it passes between system components. The solid line shows the boundaries of the overall cycle shape. The dashed-dotted line refers to the fluid stream used to reheat cold fluid headed for the primary heat exchanger. The dotted line shows the general thermodynamic region where binary coolants are divided from their gaseous phases to be pressurized separately when necessary.

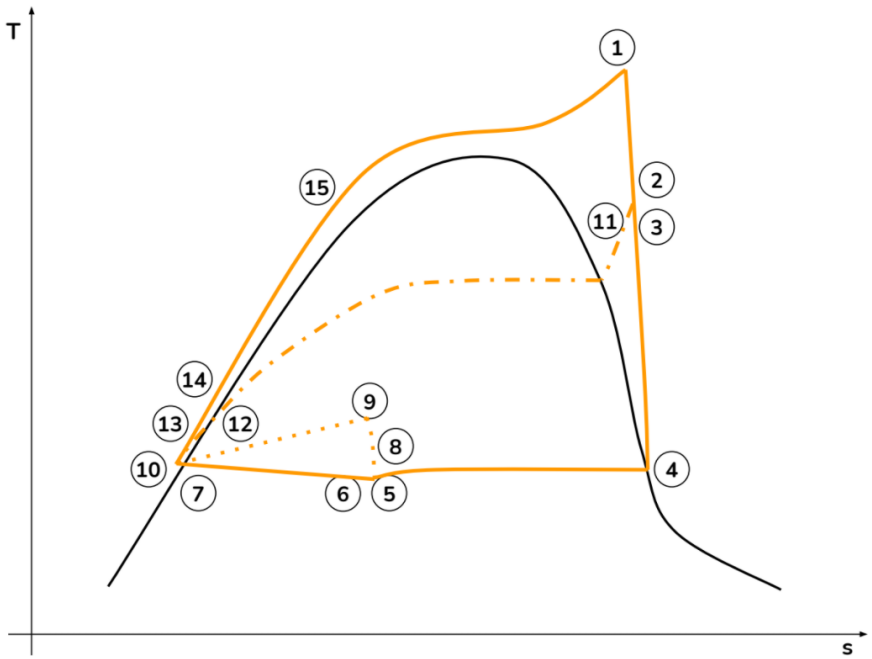

Fig. 3.2: Labeled power cycle on T-s diagram

The schematic for the cycle component design and flow is connected based on the theoretical cycle and can be reviewed in Fig 3.3. The system utilizes two expansion stages for the power extraction process. This is performed via a high-pressure (HP) expansion turbine followed by a low-pressure (LP) turbine. Included after the HP turbine is flow splitting valve that redirects a percentage of the coolant for regenerative reheating purposes.

To reliably and accurately calculate rapidly changing thermodynamics states of the fluid and extract pertinent properties, the `Python` wrapper for the open-source thermophysical property library, `CoolProp`, is employed. The library allows for quick determination of physical properties of pure and mixed fluids which are used in calculations at each station. One difficulty in simulating this system is the issue with determining fluid and mixture properties in poorly- or undefined regions, such as near the fluid supercritical point. This problem made calculating certain thermodynamic states inaccurate or sometimes impossible due to the EoS-based approach of the `CoolProp` wrapper and its database. This issue was alleviated via hard-coded error handling for these cases. When presented with this error, weighted averages of individual fluid component properties where calculated when the mix-

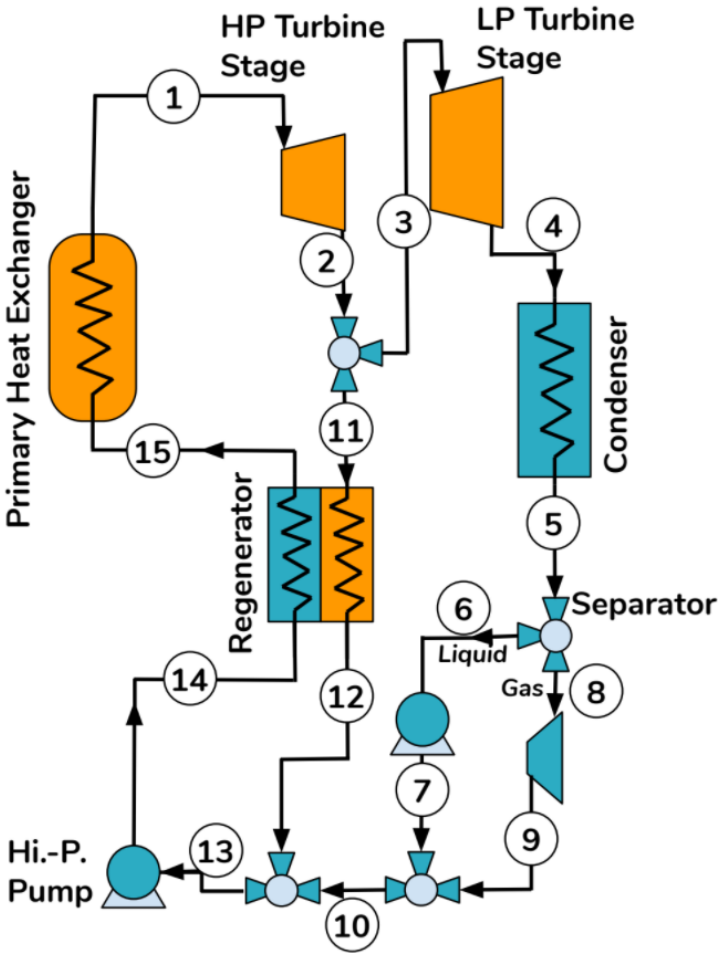

Fig. 3.3: Flowchart of the novel power system component layout

ture's could not be directly determined. This was then carried through as a noted "penalty" for that specific iteration. This penalty indicated a violation of constraining parameters or thrown error in calculations. Since the value of the penalty was not incorporated into any objective function, it is used an an integer count of issues used to aid in debugging and amending the model.

A `Python` model comprised of the mixture fluid cycle and the primary heating cycle are combined to evaluate the cycle performance. A convergence-based iterative calculation is employed to solve the complex non-linear system of equations. The basic process flow of the model can be viewed in Fig 3.4 and the general equations used are collected in the following subsection 3.1.2.

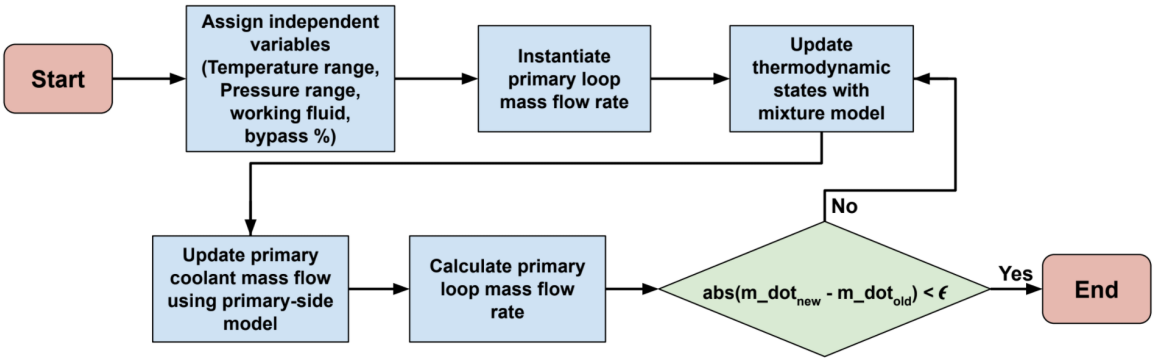

Fig. 3.4: Flowchart of the simplified solver algorithm

A number of assumptions are made for the thermodynamic model:

- The system operates at steady-state conditions
- No pressure drop occurs through the system components
- Fluid mixtures are completely homogeneous
- There is no heat lost within or between system components

For a set of design parameters, a test is completed once the calculated mass flow rate converges to a value below a set error threshold of 2%. Upon convergence, the thermodynamic state of the working fluid is defined at each location and salient system-level performance measures can be calculated. Values of system independent variables determine the overall shape of the thermodynamic cycle and are shown in Table 3.1.

Table 3.1: Bounds on independent values for cycle operating conditions

Name	**Variable**	**Value**	**Unit**
Nominal Heat In	$\dot{Q}_{in}$	160	[MW]
Turbine Efficiency	η_t	0.85	[-]
Pump Efficiency	η_p	0.75	[-]
Compressor Efficiency	η_c	0.70	[-]
Maximum Temperature	T_{max}	301	[°C]
Minimum Temperature	T_{min}	41.67	[°C]
Maximum Pressure	P_{max}	15.48	[MPa]
Baseline Cycle Output	$\dot{W}_{base}$	50.8	[MW]

3.1.2 Model Equations

The performance of the power cycle is evaluated by weighing the overall net power produced by the cycle in combination with the 1st law efficiency of the cycle. The efficiency is derived from the general steady-state equation for an open system ignoring kinetic energy and gravitational effects and shown as 3.1.

$$0 = \dot{Q} - \dot{W} + \sum \dot{m}_{in} h_{in} - \sum \dot{m}_{out} h_{out} \tag{3.1}$$

Here, h represents the specific enthalpy of the fluid. The standard convention is assumed that heat transferred into the system and work produced by the system are positive values, while the converse follows for negative values. The model equations for each component in the system design used to determine these performance variables are as follows: The work produced by the turbine is calculated via:

$$\dot{W}_t = \eta_t \dot{m}(h_{in} - h_{isen,out}), \tag{3.2}$$

which is equal to the mass flow of the fluid multiplied by the specific enthalpy change in the fluid and the turbine's efficiency. Turbine efficiency is fixed for the study at 85%. Similarly, the required work for the pump is defined as:

$$\dot{W}_p = \frac{\dot{m}(h_{in} - h_{isen,out})}{\eta_p}, \tag{3.3}$$

which is equal to the mass flow rate of the fluid times the specific enthalpy change through the pump, divided by the pump's efficiency, which is fixed for the study at 75%. The work consumed by the compressor to pressurize the gaseous component of the working fluid is found by the following equation [43]:

$$\dot{W}_c = \frac{c_p T}{\eta_c} \left[\Pi_c^{(\gamma-1)/\gamma} - 1 \right], \tag{3.4}$$

where c_p is the isobaric specific heat, T is the inlet temperature, Π_c is the compression ratio, γ is the ratio of isobaric to isochoric specific heat, and η_c is the compressor efficiency.

Compressor efficiency is fixed for the study at 70%. In the case of heat exchangers, there are different categories. For the regenerative process between two fluid streams of the same coolant, the following equation is used to balance the energy exchange between two fluids:

$$\dot{m}_h(h_{hot,in} - h_{hot,out}) = \dot{m}(h_{cold,out} - h_{cold,in}) \tag{3.5}$$

The other heat exchanger condition is with a secondary coolant, such as heat from the primary heat exchanger input to the mixed-fluid cycle. The following equation is used to make the simple heat input to the system at the pertinent component:

$$\dot{Q} = \dot{m}(h_{c,in} - h_{c,out}) \tag{3.6}$$

The cycle also includes bypass lines, so both flow splitting and mixing must be accounted for. For splitting, the only change is in the mass flow rate. In order to conserve mass, the total mass flow rate entering the split must equal the sum of the mass flow rates of the two split fluid streams. This is written simply as:

$$\dot{m}_{tot} = \dot{m}_1 + \dot{m}_2 \tag{3.7}$$

For the cycle model, we define a variable ξ bounded on the interval [0, 1], which defines the percentage of working fluid mass flow diverted away from the main circulation loop through the regenerator. The flow splitting equation can be written with this variable as:

$$\dot{m}_2 = \dot{m}_{tot}\xi, \qquad \dot{m}_1 = \dot{m}_{tot}(1 - \xi), \tag{3.8}$$

where the mass flow rate for the bypassed fluid stream is $\dot{m}_2$ and the mass flow rate of fluid flowing through the main circulation loop is labeled $\dot{m}_1$. For flow recombination, the mass flow rate and the new enthalpy state will depend on the flow conditions of the incoming fluid streams. The new mass flow rate is the sum of the two incoming streams, written out as:

$$\dot{m} = \dot{m}_1 + \dot{m}_2 \tag{3.9}$$

And the new enthalpy state of the fluid is:

$$h_{new} = \frac{\dot{m}_1 h_1 + \dot{m}_2 h_2}{\dot{m}_{tot}} \tag{3.10}$$

Finally, the first-law efficiency of the system is calculated as the ratio of net power output to the heat input to the system:

$$\eta_{1st} = \frac{\dot{W}_{net}}{\dot{Q}_{in}} \tag{3.11}$$

3.2 Model Methods

To better understanding the viability of alcohols and mixtures as potential working fluids through this study, first, an understanding of the specific solubility behaviors of the pertinent mixtures is needed. Next, optimization of the compressor power input by breaking it into multiple stages is balanced with the economics of the system component. Finally, sensitivity analysis to certain independent variables including diverted mass flow, hot stream pressure, and weight fraction of the gaseous component in the working fluid is performed. The combination of these background studies aided in quantifying lesser known fluid and component behaviors. By elucidating them, a clearer insight into system performance is revealed and provides a more straightforward troubleshooting process. With this, a computational thermodynamic performance analysis is executed via `MATLAB` on a novel regenerative transcritical cycle system capable of studying the desired mixed fluids.

3.2.1 Solubility Behavior

The definite thermodynamic state of many fluid mixtures is poorly understood in theory, as fluid interactions behave with greater complexity than simple weighted contributions from individual components. A similar elusiveness of determining properties exists for fluids in their supercritical state. Therefore, reliance on experimental data allows us to

simulate fluids and their mixtures to make better estimations on their behavior in other environments. Since carbon dioxide may dissolve in an alcohol under the system design parameters, this behavior needs to be quantified so it may be accounted for in a model. Therefore, experimental data on the solubility behavior of CO_2 in alcohols from a study by Décultot is utilized in the simulation design [44].

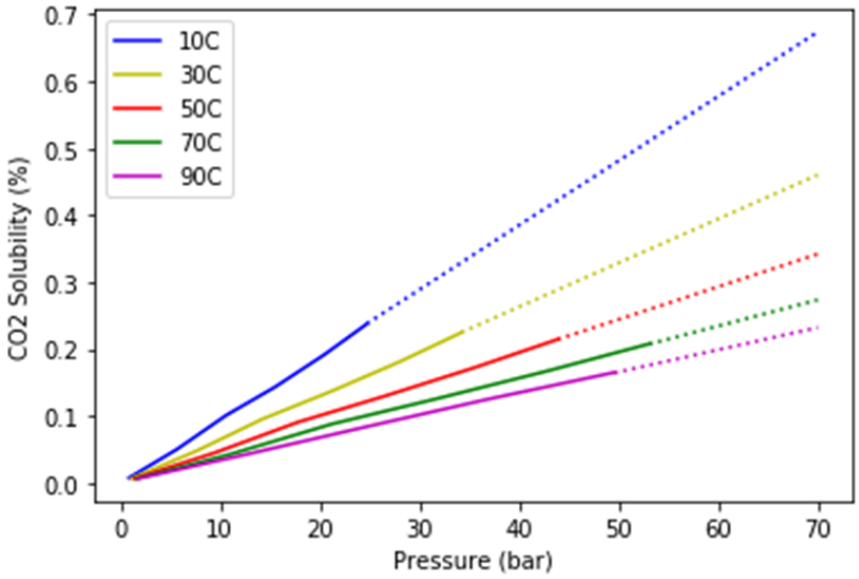

Fig. 3.5: Plot of solubility versus pressure for CO_2 in ethanol at different temperatures

Since pumps can generally pressurize a liquid at significantly lower energy costs than a compressor can pressurize a gas – and with more preferable component efficiency – an optimized design of gas pressurization can quickly benefit the total system efficiency by lowering parasitic power loss from the compressor. Data from the Décultot study [44] was used to quantify the solubility behavior of CO_2 in both methanol and ethanol. This was selected due to the robustness of the collected data within the pertinent pressure and temperature ranges of the transcritical system, which solubility is generally very sensitive to. The solubility data from the study for CO_2 in ethanol are shown in Fig 3.5. The published data extracted is shown with the solid line, while the dotted line shows an extrapolation of the solubility percentage up to the transcritical cycle P_{max} parameter.

The data from the study showed, for a given temperature, a clear linear dependence in solubility versus pressure for carbon dioxide in both alcohols. It was considered acceptable for the extrapolation procedures to consider solubility behavior of the gas outside the pressure bounds given in the study due to the robustness of the data and the lower dependency of pressure on solubility when compared to temperature. The temperature range for the simulated cycle was always inside the bounds of the experimental data for condensation and bottoming out processes. Furthermore, the system could theoretically support up to 40%wt CO_2 in a binary mixture with an alcohol. This would be the upper bound where a fully dissolved gas was still achievable at station 13 allowing for final pressurization using only a pump.

3.2.2 Compressor Optimization

As briefly mentioned, optimizing the compression process of a component gas can lead to a significant decrease in lost cycle power. This process occurs between station 8 and station 9 when referring back to the system flowchart in Fig 3.3. The flowchart indicates a simple split in the fluid between the liquid and gas phases before each is separately pressurized up to the prescribed pressure of the regenerative fluid stream (station 12). In this way, calculations are simple, but lead to extremely high power requirements for the compressor. To remedy this, compression was performed in "stages" with pressurized gas being incrementally dissolved back into the fluid stream. The overall power based on this approached was analyzed. The CO_2 solubility data from 3.2.1 was utilized to perform such analysis.

The effective idea is that before fluid enters the pump or compressor (station 5) it is separated into its individual gas and liquid phases. The gas is partially pressurized, reintroduced into the liquid alcohol via a sparging process, then this fluid is separated again. This is repeated until the gas is fully dissolved and the mixture can be pumped entirely as a liquid. Each subsequent partial pressurization (stage) has less gas to compress due to incremental dissolution into the liquid phase. By breaking down the overall pressure interval necessary to fully-dissolve into stages, less power could be consumed by gas compression.

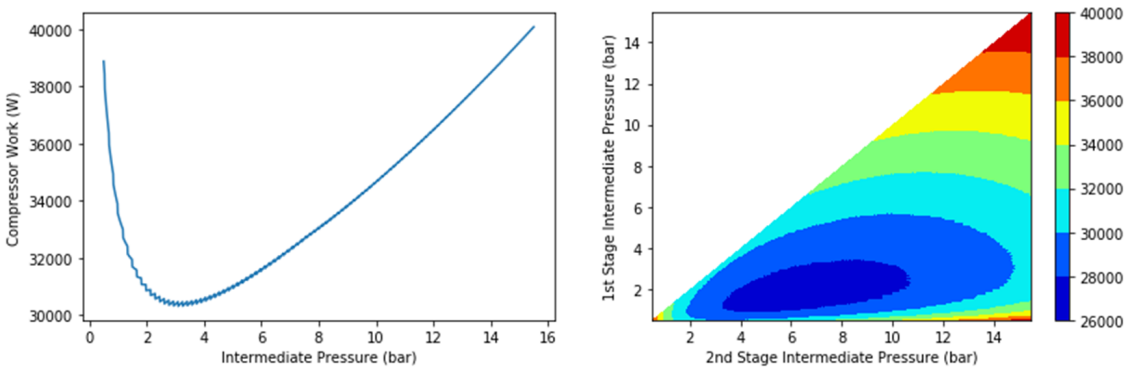

(a) 2-stage compression power (b) 3-stage compression power

Fig. 3.6: Comparison of required compression power for set pressure interval for a 2- and 3-stage compression process

The optimization methodology takes a discretized version of equation 3.4 that uses a specified number of compression stages. This method considers changes in the fluid temperature, the properties that vary with temperature (e.g. specific heat), and necessary final pressure to ensure all gas is soluble at the compressor outlet. The plots shown in Fig 3.6 show the evolution power costs when adding additional compressor stages.

The x-axis of Fig 3.6(a) can be considered a slider for the pressure value that the stages are separated by, with the overall power consumption on the y-axis. With the 3-stage process in (b), both axes are now separate sliders with the total power visualized as a heat map. Upon adding more stages, the data is more difficult to visualize in a 2-D diagram, but a consistent global minimum in consumed power persists.

The trend in compressor power reduction for a 30%wt CO_2 component in EtOH for a fluid mass flow rate of 200[kg/s] is shown in Fig 3.7. The addition of a second stage has a great benefit in power reduction, but clearly additional stages, while beneficial to saving power, are plagued by diminishing returns. Theoretically in this case, the requisite power from a single-stage compression could be reduced by nearly 40%. Considering the increase to the complexity of the system with a large number of compressors for different stages, a 4-stage compression process - which still reduced power here by 37% - is heuristically chosen for the remainder of the study.

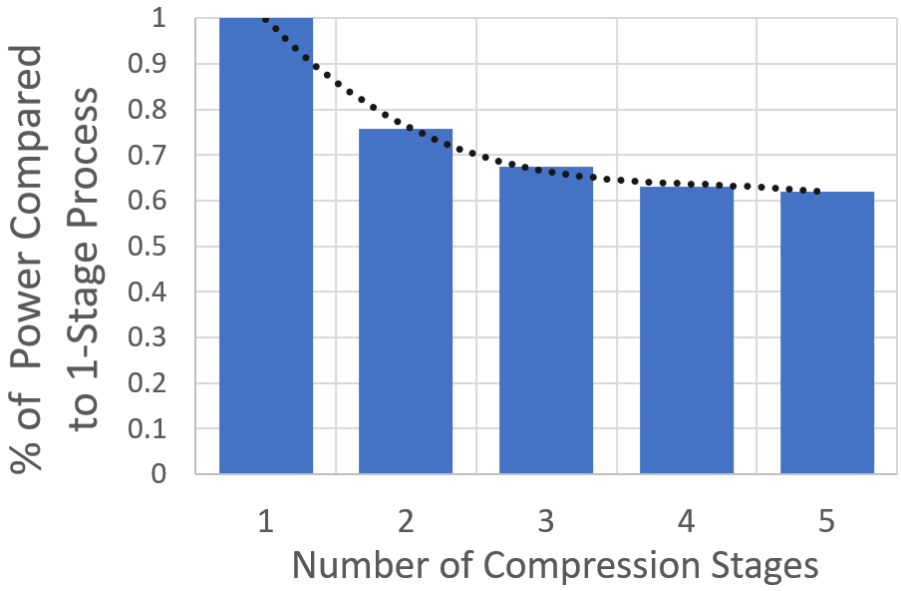

Fig. 3.7: Trend in compressor power reduction for additional stages

3.2.3 Heat Exchanger Analysis

Sensitivity analysis to specific component metrics is helpful when processing data and making changes when instantiating a new test iteration for evaluating the system performance as a whole. Cycle parameters of interest that can be tuned to optimize cycle efficiency include ratio of components in the binary mixtures used as the working fluid, the pressures through each cycle loop, and the percentage of fluid flow diverted through the regenerator. Through a series of parametric sweeps, the trends in high-level performance is analyzed when varying these metrics for the regenerator.

One sweep is visualized in Fig 3.8 where the temperature profiles for fluids streams are plotted for different amounts of coolant diverted through the regenerative heat exchanger.

The heat exchanger is discretized into 100 sections of equal length. This specific example is for an ethanol fluid mixture with 10% CO_2 by weight. The low-pressure stream is the diverted coolant used to preheat the fully-condensed high-pressure stream, and always follows the same prescribed temperature glide. Each other glide represents the high-pressure stream temperature glide for different bleed-off ratios - the percentage of the working fluid diverted from the main loop after the high-pressure turbine between stations 2 and 11.

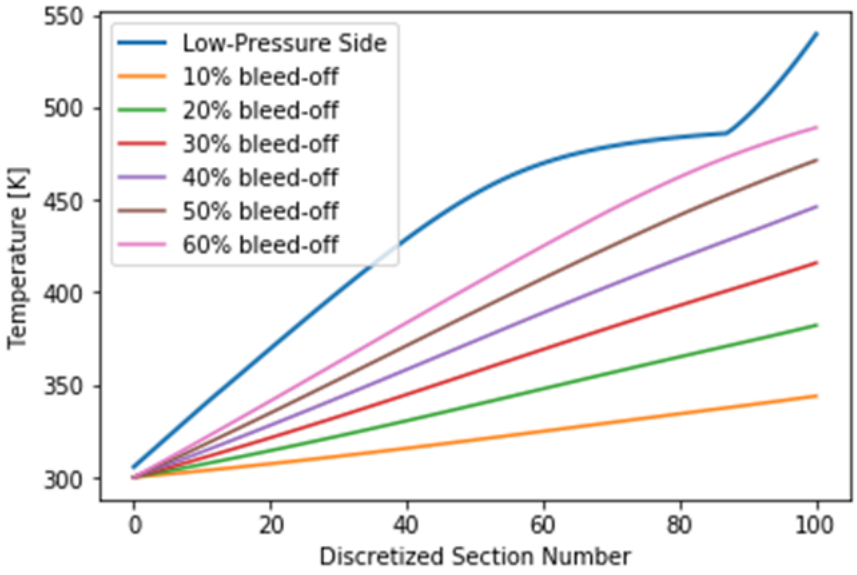

Fig. 3.8: Plot of temperature glides for fluid streams in regenerator for different mass fractions of CO_2 in EtOH

The temperature glide is directly dependent on the amount of diverted coolant, with the high-pressure stream outlet temperature increasing by about 5°C for every additional percentage of coolant diverted. This is used to inform the model by helping to keep a consistent temperature difference between the two streams for the entire length of the regenerator.

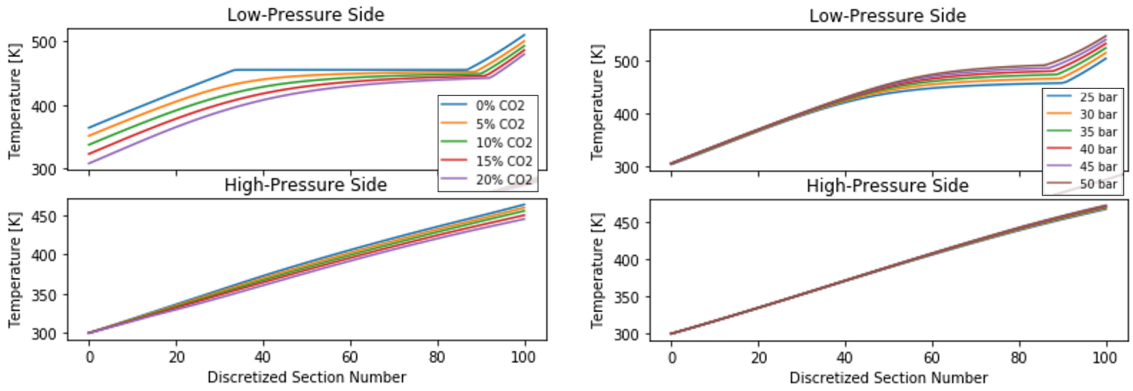

(a) Varying wt% CO_2 of coolant

(b) Varying pressure of hot-stream

Fig. 3.9: Plots of regenerator fluid stream temperature glides for parametric sweeps of other variables

The evaluation of additional variables are shown in Fig 3.9. In (a) the amount of CO_2 in the working fluid is varied and the effect on the separate fluid stream temperatures through the regenerator is plotted. Plot (b) shows the similar effect but the variable changed is the outlet pressure of the primary turbine. The thermodynamic state of the low-pressure fluid stream exiting the regenerator was fixed to be fully liquid. Clearly, these variables have a less significant effect on the high-pressure stream temperature than does the bleed-off ratio in Fig 3.8 but greatly affects the temperature glide on the low-pressure side. This is especially true for variable mixture ratios in the coolant as consistent sensible heating occurs through the two-phase region.

The maximum pressure of the system was also allowed to be variable. This was due to the changing critical pressure dependent on the component ratios of the working fluid. Higher mass percentages of CO_2 in an alcohol would raise the critical pressure. Therefore, a higher pressure ceiling was needed for these mixtures to continue running a transcritical cycle.

During all of these test iterations, it is assured that the low-pressure stream exits the regenerator as a fully-condensed liquid. This is necessary so that the fluid stream is easily combined with the incoming fluid stream from station 10 in the main circulating loop.

Generally, low flow diversion (10-30% of overall flow), low pressure ratios in the first HP turbine (4-12), and maximum pressures just above the working fluid's critical pressure (5-15% above P_{crit}) provided the most desirable regenerator temperature profiles for the pure fluids and mixtures investigated. Attentive tuning of each parameter was incorporated to optimize the regenerator as system-level performance analysis proceeded.

3.3 Results

A parametric model is devised for this system similar to the regenerator study in determining the sensitivity of the cycle performance to variations in specific operating parameters of the system components. These independent variables include: maximum system pressure (P_{max}) with an allowed ceiling of the sum of the fluid component's critical pressures, percentage of fluid diverted from the main loop through the regenerator (ξ) limited to 50%,

the pressure ratios of the HP and LP turbines (Π_1 and Π_2 respectively), and the component of CO_2 by weight in the working fluid mixture up to 30%.

A nonlinear solution scheme between the primary heat exchanger and the transcritical cycle model is designed to evaluate the overall cycle performance through optimization of the theoretical net power output for a set of parameters. A grid search is performed over the full range of each independent variable except the mixture ratio. The bounds for each variable are either prescribed by the original model description or informed through the methods evaluating specific system components in the previous sections. The remaining variables - including the primary and secondary side mass flow rates, minimum cycle pressure, and first-law efficiency - are left dependent.

Model performance for a specific coolant fluid mixture was of particular interest. Multiple optimization iterations, starting with pure alcohol coolants and then combined with a CO_2 component, are separately performed so that the performance metrics can be compared alongside each other. Mixtures with a CO_2 component combined with ethanol and methanol are optimized for the cycle. The optimized parameters for each specified working fluid are collected in Table 3.2.

Table 3.2: Optimized system data for chosen pure fluids and mixtures

Main Fluid [-]	$\%CO_2$ [%]	P_{max} [bar]	Π_1 [-]	Π_2 [-]	Bleedoff [%]	$\dot{W}_{net}$ [MW]	η_{1st} [%]	$\dot{W}_c$ [MW]	$\dot{W}_p$ [MW]	$\dot{m}_{bulk}$ [kg/s]	$\dot{m}_{regen}$ [kg/s]	T_{in};ΔT [°C; °C]
Ethanol	0	94.0	9.1	53.1	19.0	52.14	32.6	N/A	1.9	185.2	35.2	137.4; 74.4
Ethanol	10	136.5	8.3	84.1	15.0	47.11	29.5	5.1	3.1	228.2	34.2	135.4; 51.8
Ethanol	20	100.3	5.0	103	10.0	43.65	27.3	13.3	2.1	221.9	22.2	144.6; 52.9
Ethanol	30	100.9	4.4	118	32.7	34.38	21.5	19.7	8.6	323.9	105.9	143.6; 81.0
Methanol	0	85.5	7.1	31.2	23.7	54.09	33.8	N/A	2.2	140.4	33.3	141.1; 88.8
Methanol	5	87.1	15.9	14.3	33.0	49.51	31.0	2.1	3.8	175.7	57.9	140.9; 67.2
Methanol	10	88.8	12.5	18.5	14.0	47.37	29.6	4.6	3.2	153.5	26.1	146.3; 53.5
Methanol	20	88.3	4.76	48.3	13.1	45.49	28.4	10.6	2.8	169.3	22.1	145.5; 42.6
Methanol	30	96.6	4.73	53.2	29.0	40.42	25.3	12.9	5.0	251.8	73.0	142.2; 69.0
Methanol	30	154.8	5.56	73.1	34.0	38.53	24.1	14.1	7.6	295.9	100.6	147.8; 71.9

Along with the optimized variables, included in Table 3.2 are some other parameters that inform performance of some specific components. These parameters include the work consumed by the pumps and compressors, the converged mass flow rate of the working fluid

in the main loop, the mass flow directed through the regenerator, and the inlet temperature and temperature increase through the regenerator for the high-pressure stream.

Many aspects of the system are coupled with each other. For example, higher values for ξ diverts gas from the compression process and leads to a reduction in consumed compressor power. Because of coupled behaviors, the ability for the model to converge to an optimal solution were heavily dependent on the initial guess for independent variables when initializing the model for a specific mixture. Divergent test cases were used to inform better initialization of a test iteration.

Based on the model, a pure MeOH working fluid provides the best performance for the designed cycle, achieving a first law efficiency just shy of 34%. Performance of MeOH mixtures with an equivalent concentration of CO_2 to a similar EtOH mixture also provided better cycle efficiency in every case. The superior performance over ethanol was also achieved at a lower maximum pressure, which has positive consequences on the economics of a physical system.

A few trends were clear from the tabulated data. Generally, the pure fluids performed better at preheating the high-pressure stream for the primary heat exchanger. This could then allow for better heat transfer via a greater thermal conductivity and utilizing increases in specific heat in the pseudo-critical region of the fluid. The pure fluids, while omitting the necessity of a compressor, also required low power for the pump compared to mixtures. This was not always true for MeOH though, but with the necessity of a compressor, mixtures always required more power for processing the coolant back to a high-pressure state. Generally, mixtures with a larger CO_2 component could support larger overall mass flow rates for the cycle. Most notably with mixtures was the exponential increase in the requisite power for the compressor with an increasing CO_2 component. This parasitic power loss was likely determinant in the consistently decreasing power output and cycle efficiency for an increasing CO_2 component. More salient metrics regarding this are detailed in Table 3.3.

The effect of increasing compression power was greater exacerbated in ethanol mixtures, which also required higher maximum cycle pressure in nearly every case. These consequences

Table 3.3: Optimized system-level resulting data for selected working fluids

Working fluid	$\eta_{\mathbf{1st\text{-}Law}}$ [%]	$\mathbf{P_{max}}$ [MPa]	**Ratio of** $\mathbf{P_{comp}/P_{out,net}}$
100% MeOH	33.8%	8.6	0%
90% MeOH + 10% CO_2	29.5%	8.9	9.74%
80% MeOH + 20% CO_2	28.4%	8.8	23.3%
70% MeOH + 30% CO_2	25.3%	9.7	31.9%
100% EtOH	32.6%	9.4	0%
90% EtOH + 10% CO_2	29.5%	13.6	10.8%
80% EtOH + 20% CO_2	27.3%	10.0	30.5%
70% EtOH + 30% CO_2	21.5%	10.1	52.7%

further supported the benefits of continuing an evaluation of methanol-based coolants for the model. Yet in all cases, the system was shown to be effective at pulling sufficient thermal energy from the primary side nuclear heat source at or greater than the original prescription of 160[MW]. The ability for this transcritical model to pull a large amount of heat favorably demonstrates the effectiveness of this cycle design for use in small, decentralized power generation.

While the first-law efficiency is indicative of effective cycle performance, it does not reveal all the nuance of working fluid behavior. Due to cases where weighted averages of physical fluid properties are utilized - such as the specific heat when limitations in theoretical data persist and calculations with non-ideal mixtures are inaccurate - the cycle efficiency from the model is only indicative of the relative theoretical thermodynamic potential of each working fluid in the power cycle. Furthermore, it is unknown how some thermophysical effects of present gases, such as convective heat transfer enhancement from bubbles in the heat exchanger, affect the overall cycle performance. In a physical prototype, heat transfer performance may increase from turbulence phenomena. Due to the nature of this model, the added gas merely adds a consequence of consuming more power.

Further study can dive deeper into such nuances of the system to better elucidate real-world physical operating behavior of an alcohol-based mixed fluid cycle. Due to many rigid constraints and bounds on the cycle model, investigation into the specific working fluid thermophysical characteristics is left as the most significant unknown. With promising simulation results, the next logical step is to procure experimental data that will further develop

the lacking documented thermal transport properties of desirable fluids and ancillary mixtures, which suffer from poor universal tools for theoretically calculating data in complex energy systems [45]. Therefore, avoiding complete necessity on theoretical calculations, physical analysis will allow for the determination of the maximum thermal energy exchange capabilities of these working fluids under loads that may perform better than common steam-based systems. These innovations may unlock new ways to incentivize small modular reactors and micro-reactors as the primary method to meet current energy demands in a sustainable manner.

CHAPTER 4
EXPERIMENTAL HEAT TRANSFER PERFORMANCE VALIDATION

4.1 Project Overview

Utilizing the simulated model will, at a bare minimum, help us understand the thermal flow behavior of the organic fluid under pseudo-supercritical conditions to support designing a physical experiment to validate our data. However, physical heat transfer behavior always behaves with more nuance than can be completely explained by theory. Therefore, a physical analysis is desirable. A common architecture in thermal transport experiment design is analyzing fluid flow through a channel, and will act as the next crutch to elevate an understanding about supercritical fluids in this application. For this experiment, we aim to better understand how well (or poorly) supercritical fluids can act as a coolant for a power cycle application. Characterization of the dynamic heat transfer properties of a working fluid is done by controlled heat input and temperature measurement. A methodological approach to isolating the pertinent variables is derived by combining aspects of those outlined by separate experiments by Pu, Wang, and Kromer [46–48].

While a good estimation can be generally made, there is a clear deviation from the known physical behavior from theoretical calculation of thermal transport properties. Determining the useful thermal transport behaviors of a working fluid (i.e. optimizing the Nusselt number in heat exchanger architectures) first requires a high-level understanding of the working constraints, such as the fluids thermodynamic state and flow conditions, that best provide this. Therefore, we have great support to further isolate and determine the thermophysical state and properties of certain fluids existing in these regions.

The desired thermodynamic state of the fluid of interest is isolated within the experimental test section, which houses the bulk of the data acquisition devices in the system. The balance of systems in the experimental apparatus ensures the preparation of the desired

thermodynamic state in addition to the cool-down upon exit, stable pressure, and controlled flow rate of the fluid through the test section. The test section is affixed with resistance heating elements to provide flux into the fluid. The material and geometric designs considered when fabricating the test section component allowed for the desired fluid flow conditions desired for analysis of specific heat transfer behaviors and steady-state development.

By taking reliable temperature data from a changing phase or supercritical fluid flow, we can determine local spacial heat transfer behaviors and how it changes with variations in heat flux, pressure, or mass flow. The small scale system is designed make accurate measurements of pressure, temperature, and heat flux to derive predictions of thermo-physical properties and of the Nusselt number under controlled constraints. This will illuminate characteristics of the supercritical fluid's convective heat transfer behavior and aid in comparing benefits of supercritical fluids to two-phase heat transfer. Thereafter, these techniques can be extrapolated to other fluids and pave the way for modifying these systems uncommonly used fluids, such as heavier polar compounds or siloxanes, that pose similar desirable thermodynamic properties and/or economically feasible traits at supercritical conditions. This can be realized in lower operating pressures or safety concerns, reducing capital investment and public fears.

4.2 System and Components

Certain components of the experiment required advanced simulation and special fabrication to ensure desired performance in fluid flow behavior and thermophysical states. These mainly included the test sections containing the bulk of the systems data acquisition hardware. Following thereafter is the construction of the test facility for balancing the system with this controlled heat exchanger.

4.2.1 Alpha Test Section Design

The alpha prototype heated test section is designed for flowing R134a (and possibly other similar non-corrosive fluids) with its dimensions diagrammed in Fig 4.1. The main structure consists of a mirrored top and bottom plate sandwiching the flow channel in

between. The only difference between the plates are the top posses two ports for incoming and outgoing fluid flow, while the bottom contains fluid wells below each port to aid in flow uniformity at the inlet. Each plate contains 20 fins which "discretely" conduct heat from the source to the fluid. The plates are constructed out of 6061-T6 aluminum with an overall length of 222.25[mm] and a heated length, L, of 105[mm]. The two fins at the edges of the heated length have a thickness, $t_{f,end}$, measuring 5.5[mm], while the thickness of the rest, denoted t_f, measure 3[mm]. All of the fins are the same height (h_f) and width (w_f), measuring 15[mm] and 19[mm] respectively, and are separated by a length s_f measuring 2[mm]. Fixed to the upper surface of both fin arrays are a copper block each housing a resistance heater. The fins are designed to discretize the flow of heat conducted from the heated copper blocks to the fluid in the channel. The fins are also equipped with two thermocouples that are installed in the upper and lower portion of each fin and spaced 10[mm] apart, allowing the heat flux through the individual fin to be quantified.

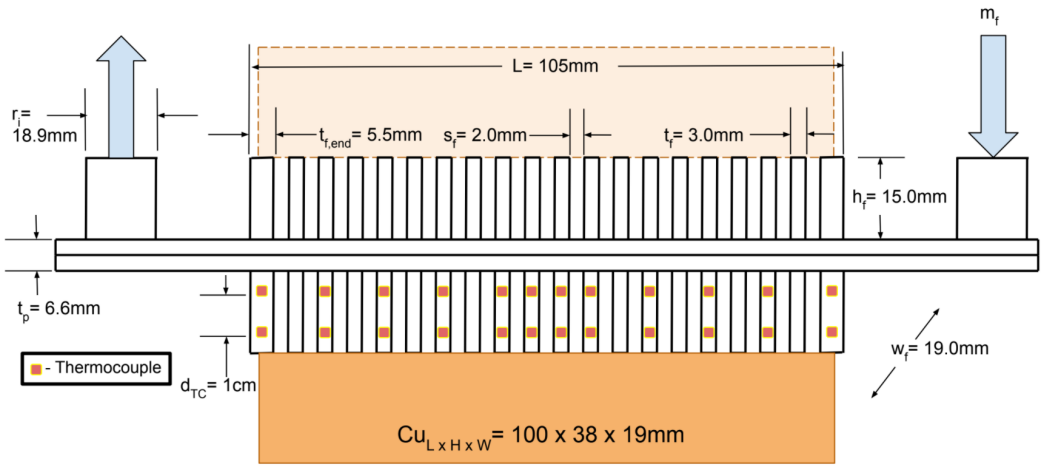

Fig. 4.1: Schematic of the heated test section for R134a

The two copper blocks are affixed to the test section via steel hose clamps and bonded to the tops of the fins using a high-temperature boron-nitride-based thermal paste rated at 31.4[W $m^{-1}K^{-1}$]. This paste is used for all metal-metal interfaces. A 1/4" cartridge heater rated for 325[W] is installed lengthwise through each copper block. The blocks are heated to a prescribed temperature setpoint maintained using an Omega CS8DPT digital

controller connected to the heaters in parallel. The setpoint is monitored by an Omega general purpose RTD bonded to the center of the lower copper block. The fluid's inlet and outlet temperature are measured directly using 1/16" Omega T-type thermocouples (SCPSS-062U-6). The same model thermocouples are installed in the fins, counting 26 total thermocouples within the test section. Pressure measurements are taken at the same fluid inlet/outlet locations as the temperatures, allowing the pressure drop across the test section to measured. Two Omega model PX319-1KAI transducers rated for 1000[psi] are used here at the inlet and outlet.

Fiberglass insulation is wrapped around the test section to fully-isolate it from the surroundings and minimize heat losses. At least 6 inches of insulation is maintained around the entire surface of the test section.

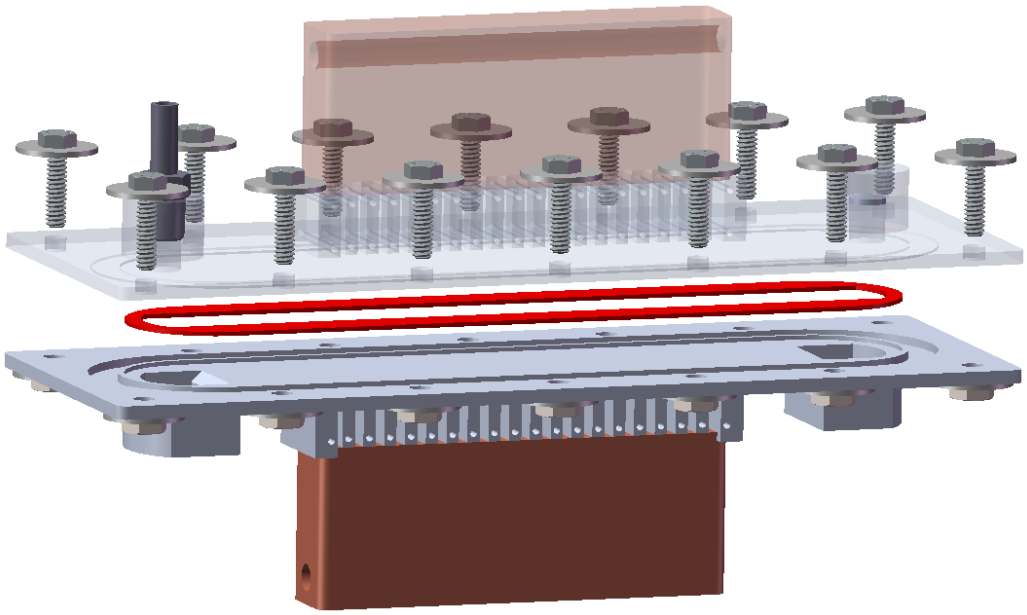

Fig. 4.2: Exploded view of the alpha test section modeled in Solidworks

An upper and lower plate house a wide aspect ratio channel for the fluid flow measuring 10[mm] wide by 1[mm] tall. The channel geometry is specified by an insert components fit in between the plates. This piece is easily identified in the `Solidworks` rendering of the test section in Fig 4.2 as the central component in red. A channel insert is chosen in order to

preserve modularity of specific channel geometeries and to future proof the design for a range of flow conditions. This channel is shimmed between the plates using a high-temperature silicone sheet 0.01[in] thick to maintain a tight seal. The modeled test section is simulated under the working conditions of high-pressure flow with 1,1,1,2-tetrafluoroethane (R134a). This determines the requisite plate thickness and clamp force to ensure safe operation. Consideration is made to allow for a factor of safety 50% above the critical pressure of the refrigerant (6[MPa]) during operating fluid flow.

4.2.2 Beta Test Section Design

A beta prototype test section is designed to handle the incompatibilities between MeOH and aluminum. Higher corrosion resistance is necessary and also future-proofs this prototype to allow for a broader range of fluids to be investigated later. The test section is rendered again using `Solidworks` in Fig 4.3 and makes use of steel, copper, and aluminum components. The top and bottom plates (labeled "A" in the figure) which house the flow channel are precision machined out of 316L stainless steel. The plates measure a total overall length of 237.5[mm] with a 140[mm] heated control length. The plates are 44.5[mm] wide with the greatest thickness measuring 12[mm] at the ends and thinnest thickness measuring 2.125[mm] in the center portion containing the fins. Ten fins span the heated length of the test section with drilled thermocouple holes similar to the alpha test section design. Here, the bore holes are spaced 2[mm] apart center-to-center inside each fin for taking flux measurements. The ten fins measure 4.25[mm] thick, 10[mm] wide, and 5[mm] in height. The fins are each separated by a 2.65[mm] gap.

Two steel plates (labeled "B" in Fig 4.3) are positioned at the top and bottom of the beta test section, also fashioned from 316L stainless steel. These plates are joined using eight 1/2" bolts which provide the majority of the clamping force sandwiching the system together.

In between the clamping plates and the channel plates stand three blocks (on both sides) of copper and aluminum which all serve to guide the clamp force from the exterior plates to the interior plates to compensate for the pressurized fluid contained within the

channel. The copper blocks and larger aluminum blocks serve the dual purpose of providing clamping pressure and as heat sources for the fluid. On the top surface of these blocks, a high temperature silicone sheet is inserted between all three blocks and the steel clamp plates to increase the thermal resistance to reduce conductive heat losses to the outer plates. The copper blocks (labeled "C" in Fig 4.3) measure 79.5[mm] in length, 9.5[mm] wide, and 25.15[mm] in height. A 1/4" bore hole is drilled through the side of the block to house a cartridge heater rated for 300[W]. These blocks are positioned along the primary heated length of the test section where the majority of thermocouples are stationed. The larger aluminum blocks (labeled "D" in Fig 4.3) measure 44[mm] long, 20.3[mm] high, and 9.5[mm] wide. These blocks also have a lengthwise bore hole 1/8" in diameter which house cartridge heaters rated for 100[W]. These blocks are positioned at the channel inlet and serve as preheaters for the fluid to achieve the desired temperature as it flows through to the primary heated length. The smaller aluminum blocks (labeled "E" in Fig 4.3) are 20.7[mm] long, 20.3[mm] high, and 9.5[mm] wide. These blocks serve only as supports for the integrity of the test section.

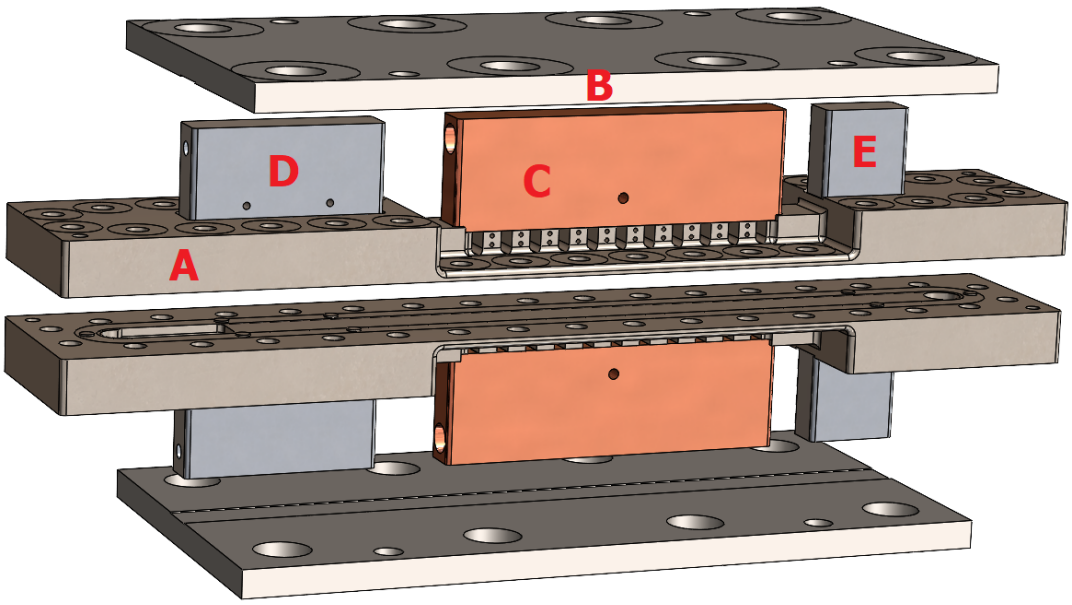

Fig. 4.3: Exploded view of the beta test section modeled in Solidworks

The channel sandwiched in between the central steel plates measures 170[mm] in length, 10[mm] wide and 1[mm] thick. Guiding pins surround the body of the milled channel at the ends and along the long edges to ensure an even thickness along the length when the plates are pressed together. A thin silicone gasket is custom cut to fit around the channel and these pins to ensure a tight seal for pressurized fluid flow.

The test section is designed for analysis at low mass flow rates on the order of grams per second. This preserves the desired flow development and thermal transitions to occur within the primary heated length of the channel, namely mixed to turbulent flow. At prescribed flow conditions, the system is designed to isolate up to a 20°C temperature increase through the channel. Maximum operating pressures up to 10[MPa] (FS of 1.2) and temperatures up to 750[K] are verified using `Solidworks` mechanical and thermal simulations. Material safety factors of at least 1.5 are maintained with respect to mechanical performance due to thermal stresses.

While the materials constructing the beta test section are determined mainly for fluid compatibility, the geometry of components are specifically designed for heat transfer performance from the heaters to the fluid. This is most notable with the central stainless steel plates which possess a significantly lower thermal conductivity than the copper and aluminum components. The geometry of these plates is such that the most significant thermal resistance is maintained within the fluid itself compared to the conducting thermal network from the heater to the fluid channel within the test section.

Similar devices to the alpha test section are used for measurement of pressure and temperature. Two Omega PX319-2KAI transducers rated for 2000[psi] measure fluid pressure directly at the inlet and outlet of the test section. The same 1/16" Omega T-type thermocouples are inserted within the bore holes of each fin to measure surface temperatures are for quantifying heat flux through each discrete fin. Two of the same thermocouples also directly measure the fluid temperature at the inlet and outlet adjacent to the transducers. Three 10[μm] fine gauge thermocouples are fit in between the test section plates to directly measure the temperature of the fluid contained in the channel at discrete points along its

length. Bulk fiberglass insulation materials is again used in the same manner as the alpha test section with at least 6[in] of insulation packed in to surround the test section.

4.2.3 Bench-Top Test Facility

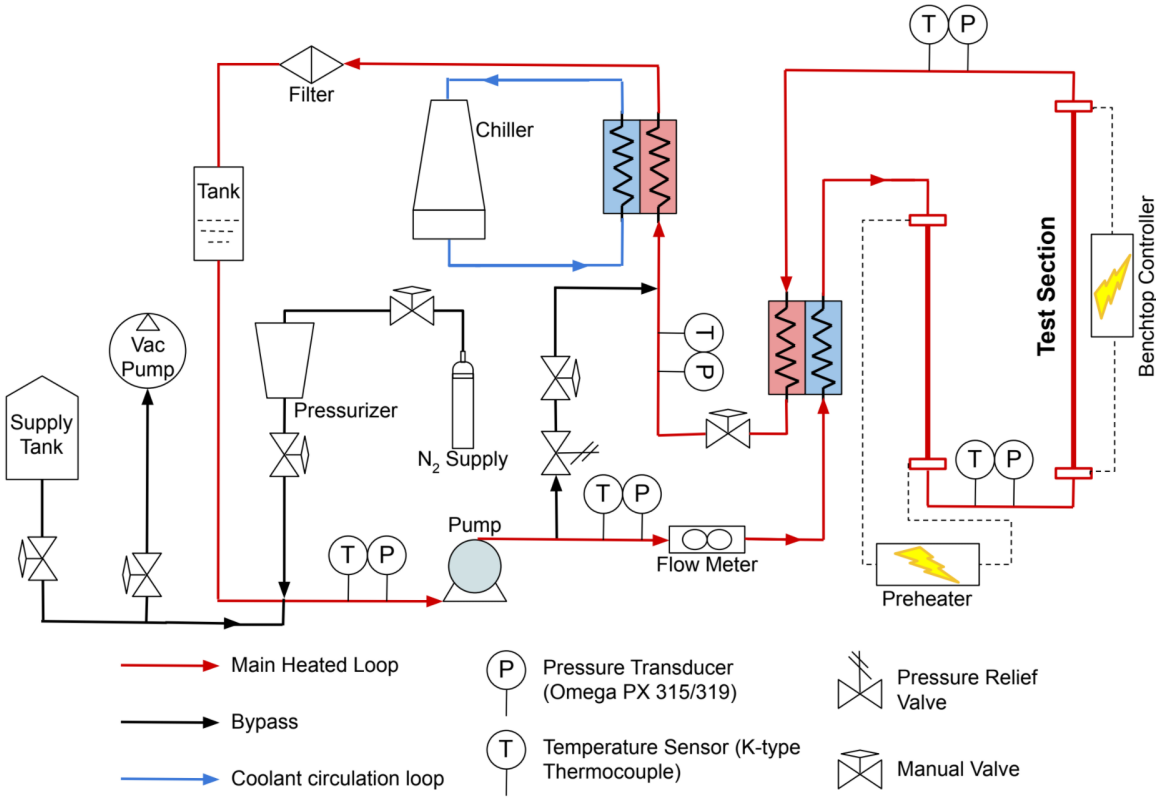

Fig. 4.4: Schematic of the experimental loop bench-top facility

The basic layout and flow of the experimental apparatus design is shown in Fig 4.4. The main circulation loop, shown in red, consists of a piston pump, a flowmeter, a recuperative heat exchanger, an electrical resistance preheater, the heated test section, a condensing heat heat exchanger, a refrigerant filter/dryer (applicable to alpha test section), and a collection tank. The connections between system components are custom made using bulk smooth-bore seamless 304 stainless steel tubing (1/4" OD, 0.028" thick walls). The supercritical working fluid is circulated through the loop via the pump (Parker Hannifin 5-piston pump model HR865B) driven by a model PD-441-1001 24VDC permanent magnet motor. The

mass flowrate of the fluid is controlled via the power input to the pump. The specific current and voltage input to the pump is regulated using a SOLA SDN 20-24-100P power supply. Needle valves in the main heated and bypass loops are also utilized to provide restriction and redirection of flow when necessary. Swagelok model SS-1RS4 needle valves are in place for all the manual valves in the apparatus. The volumetric flow rate is measured with a positive displacement flowmeter (AW-Lake JVA-12KG-25-NPT).

The recuperator saves energy by absorbing heat from the fluid exiting the heated test section, then enters the preheater where the temperature is elevated to the desired value at the entrance of the test section. Fluid from the test section outlet preheats incoming fluid via the recuperator before entering the condenser. Once cooled to a liquid, the fluid is filtered and enters the loop storage tank.

The chilling loop, shown in blue, consists of a Thermo Scientific NESLAB RTE 7 circulating bath pumping a cold propylene glycol alcohol-based HTF at a prescribed setpoint to maintain consistent condensation of the working fluid. The bypass loop, shown in black, is managed by an emergency pressure relief valve (Parker Hannifin 4A-RH4A(-VT-SS-K2) series) which establishes the ceiling for the pump's output pressure. A manual control valve follows which is used for flow redirection. Pressure and temperature measurements are taken at multiple points in the test loop. Measurements are taken at the pump inlet and outlet, the test section inlet and outlet, and the inlet to the condenser. Temperatures are measured using the same Omega T-type thermocouples as the test section and the pressure transducers used adjacent to the test section are specified in their respective sections. The remaining pressure measurements in the loop are acquired from Omega PX315-500GI pressure transducers. These are in place to ensure that desired thermodynamic states and safety margins are met. The flowmeter and pressure transducers are all powered using a New Focus $\pm$ 15V model 0901 laboratory power supply.

The closed loop is connected to a bulk working fluid storage tank, a Varian T-series turbo vacuum pump, and a nitrogen cylinder at a manual manifold. Here, the desired fluid is charged into the system from bulk storage. Prior to charging, the turbo vacuum pump is

used to evacuate the entire system of impurities and create negative pressure. The nitrogen tank is used to purge the system after each test iteration and for storing the system safely for extended periods.

The general working conditions ranges for the whole system can be reviewed in Table 4.1 for flow tests performed with both the alpha and beta designs of the test section.

Table 4.1: Experimental apparatus design parameters

Parameters	**Value/Range**
Max design pressure	10.0 [MPa]
Low-pressure side	0.4 [MPa]
Design temperature	100-350 [°C]
Volumetric flow rate	0.25-10 [mL/s]
Heating capacity	650-800 [W]
Chilling capacity	500 [W]

4.3 Experiment Methods

The following sections outline the procedures for acquiring data from the bench-top experiment facility and processing of the raw data into useful measures.

4.3.1 Data Acquisition

Data is acquired from the benchtop apparatus using technology developed by National Instruments. A cDAQ-9189 chassis houses modules specific to the data acquisition device: two NI-9213 provide for the 29 thermocouples, an NI-9203 provide for the six current signals (transducers and flow meter), and an NI-9216 module measures RTD temperature devices. The measured signals are compiled using a `LabVIEW`. The flowchart for general process of the data acquisition program is shown in Fig 4.5.

Two physical channels are created each for temperature and current signals. These channels feed through a timing digitizer that helps enhance the data sampling rate. From here, both channels feed into a while loop along with a run-time counter designed to halt at user input. Once the program is initiated, the acquired signals are fed into arrays the

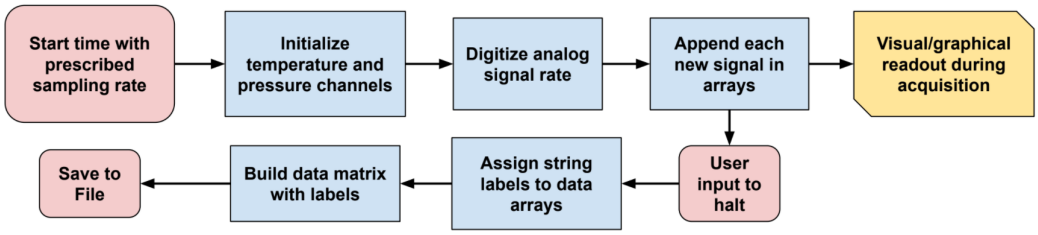

Fig. 4.5: Flow diagram of the simplified data acquisition program

continuously append each new datapoint. The temperature signals are directly interpreted by the program after, however the devices with current signals required direct conversion using their calibration curves. As data is appended, plots of the pertinent operational data for the system is read-out over time. This is used to manage the state of the system and fluid during a test iteration.

Once the program is halted, the user is prompted whether to save the data to file. When prompted to save, labels are assigned to each individual signal for later identification and the data are built into a single large matrix of 36 variables. The tab delimited batch file is then easily read into a dataframe for post-processing.

The specific channels to measure and the desired data sampling rate for a test iteration are specified at the user interface prior to running.

The entirety of the visual-based programming block diagram for data acquisition can be referenced in Fig B.1.

4.3.2 Equations

Using the compiled data from `LabVIEW` from each test iteration, the characterized fluid properties are calculated in a `Python` script. Characteristics of the fluid flow behavior and heat transfer regimes are better understood using common dimensionless variables including the Reynolds number:

$$Re = \frac{\rho u D_h}{\mu} = \frac{4\dot{m}}{\mu P}, \tag{4.1}$$

where D_h is the hydraulic diameter of the flow channel and P is the perimeter of the channel cross-section. The Nusselt number:

$$Nu_L = \frac{hL}{\lambda} = \frac{hD_h}{\lambda}, \tag{4.2}$$

where h represents the convective heat transfer coefficient of the fluid and L is the length over which the Nusselt number is quantified, here being the hydraulic diameter of the rectangular channel. This length is usually taken as the portion of the channel for which a discrete fluid packet flows through. And the Grashof number:

$$Gr = \frac{(\rho_s - \rho_b) g D_h^3}{\rho_b \nu^2} \tag{4.3}$$

The development length for each test section is determined by the desired flow condition at the inlet to the heated length. For laminar flow:

$$x_{dev,lam} = 0.05Re \cdot Pr \cdot D_h \tag{4.4}$$

For turbulent flow:

$$x_{dev,turb} = 10D_h \tag{4.5}$$

The temperature of the local fluid packet beneath each fin is calculated and compared to the experimental measurements along the channel length. This is used to determine heat transfer properties of the fluid and aid in uncertainty analysis. The temperature can be determined using a thermal circuit model of the heated test section where the the heat flux through a fin can be related to a temperature difference and an effective thermal resistance.

$$\dot{q} = \frac{\Delta T}{R_{eff}}, \tag{4.6}$$

and a single conductive resistance is quantified by:

$$R_{cond} = \frac{L}{k_{fin} A_c}, \tag{4.7}$$

where L defines the length separating the discrete temperature nodes and k is the thermal conductivity of the conducting metal medium. This quantifies a heat rate-based resistance with units [K·W^{-1}]. Similarly, the convective resistance of the fluid is quantified by:

$$R_{conv} = \frac{1}{hA_c} \tag{4.8}$$

The fluid temperature is related to the measured temperatures of the fins and the rate of heat transfer through each individual and determined through Eqn 4.9:

$$T_{f,loc} = T_{fin,hot} - \frac{\dot{q}_{loc}}{R_{eff}}, \tag{4.9}$$

where the effective resistance is the sum of all conductive and convective resistances dividing the hot temperature measurement in a specific fin and the local bulk fluid temperature beneath that fin. Radiative effects within and losses from the test section are ignored for this analysis.

For a specified setpoint temperature of the heaters, the heat rate into the fluid can be calculated in a couple of ways. The first way is via the energy balance between the thermodynamic states of the fluid entering and exiting the test section using Eqn 4.10:

$$\dot{q}_{calc,flow} = \overline{\rho \dot{V} c_p} \left(\overline{h}_{out} - \overline{h}_{in} \right) \tag{4.10}$$

Another approach is to use the flux measurements obtained with each fin passing heat from the hot blocks to the fluid channel using Eqn 4.11:

$$\dot{q}_{calc,flux} = k_{fin} A_{c,fin} \sum^{j} \frac{\overline{T_{h,j}} - \overline{T_{c,j}}}{dx}, \tag{4.11}$$

where each countable number j is the position of a fin along the length of the test section and T_h and T_c are the hot and cold thermocouple temperatures measured within that fin

respectively. With Eqn 4.11 the bulk temperature of the fluid passing through the channel can also be calculated from each local fin heat rate and the fluid mass-flow rate. A useful measure of heat exchange performance is the logarithmic mean temperature difference, shown in Eqn 4.12:

$$LMTD = \frac{(T_{out} - T_w) - (T_{in} - T_w)}{\ln\left(\frac{T_{out}-T_w}{T_{in}-T_w}\right)}, \tag{4.12}$$

where the values T_{in} and T_{out} are the local fluid temperatures at the leading and trailing edge of each fin within the channel, quantifying the discrete increase in temperature below each fin. An experimental measure of the fluid's convective heat transfer coefficient can be determined using measures from previous equations in the following Eqn 4.13.

$$h = \frac{\dot{q}}{A_s \cdot LMTD} \tag{4.13}$$

This is compared with a standard way of computing the local convective heat transfer shown in 4.14:

$$h = \frac{\dot{q}}{A_s\,(T_w - T_{f,b})}, \tag{4.14}$$

where $T_{f,b}$ is the average bulk temperature of the fluid in the channel and A_s is the inner surface area of the channel. For a fluid packet beneath a single fin, this value is the average of the T_{in} and T_{out} values from Eqn 4.12. This Eqn 4.14 is the main one used for obtaining convective heat transfer results in section 4.4.

Finally, uncertainties between the measured values and calculated metrics are determined using an L2 normalization shown in Eqn 4.15.

$$\delta R = \sqrt{\sum_{k=1}^{N} \left(\frac{\delta f}{\delta x_k}\delta x_k\right)^2} \tag{4.15}$$

4.3.3 Data Analysis

With the compiled datasets from `LabVIEW`, the data are imported into a dataframe using the `Pandas` library for simple indexing, transformations, and post-processing of the raw data. `Python` version 3.7 is the language of choice for all post-processing purposes. The general equations exposed in the previous section 4.3.2 form the basis of the analysis by extracting useful metrics of fluid behavior and performance from the data. The bulk of the scripts developed and used may be referenced in appendix section B.

The most pertinent data for heat transfer deductions is provided under system steady-state conditions. Under steady state conditions, all system parameters are assumed to be unchanging, including the mass flow rate through the test section. During steady-state intervals, measurements are averaged over time to remove complexities associated with the dynamic development period and dependence on transient changes.

The local fluid analysis seeks to determine fluid properties in discrete fluid packets beneath the fins of the test section. In addition to the steady state assumption with the system, relevant data analysis of the discrete fluid packets also quantify the following assumptions:

- The difference in specific heat between adjacent fluid packets is negligible.
- Kinetic and potential energy changes between the test section inlet and outlet are ignored.
- The pressure drop through the channel length is very small (verified by data) and the pressure is a linear decrease.
- Heat transfer into the fluid packet is equivalent and constant from both the upper and lower fins.

Steady state intervals must remain stable for a period of at least 100 seconds to be considered valid. The quantification of the heat transferred to the fluid using both Eqns 4.10 and 4.11 aid in justifying the performance of steady system operation when these values align with each other. Similarly, the mass-flow rate of the fluid can be determined using

these two methods. A test iteration is only considered problematic when the error between these values exceeds a 25% difference, which generally indicates that the fluid temperature through the channel length cannot be bounded between the inlet and outlet temperatures during a phase change process. The inlet and outlet temperatures measured directly for the fluid are used for projecting the actual fluid temperature within the length of the test section channel from the temperature measurements within the fins. The temperature values measured at the thermocouple array within the test section fins closest to the channel are used in a 1D conduction method via Eqn 4.7 to determine the local wall temperature (T_w) at the inner surface of the channel. An example of the measured thermocouple temperatures with the calculated wall temperature can be referenced in Fig A.3.

Flux measurements through fins without any attached thermocouples are assumed to possess a heat flux equal to the average flux through its adjacent fins (only applicable to 8 total fins near the inlet and outlet of the alpha test section, see Fig 4.1).

The heat transfer analysis breaks the channel into 20 discrete fluid packets where thermodynamic properties, such as the specific heat and vapor quality (when applicable), are locally computed as the fluid flows through the entire channel using the local pressure and temperature values of the fluid. An example plot of many of these local determined properties during a phase change interval may be referenced in Fig A.4. The convective heat transfer rates of the fluid are quantified and shown over the range of vapor quality during two-phase heat transfer and over the range of super-heating once a full vapor phase is achieved.

With the quantified local heat rates, fluid and wall temperatures, and convective fluid heat transfer rates, the Nusselt number for single-phase heat transfer can be determined across the length of each fin. The experimentally determined values are also compared to convective heat transfer correlations including Dittus-Boelter, Gnielinski, and Mokry et al, collected in appendix section A.2.

Additionally, the literature generally refers to a fluid existing in its supercritical state if only above both its critical temperature and pressure to establish solid boundaries. However,

the boundaries possess a gray area depending on the specific theoretical resource referenced or physical situation a fluid is applied to. According to the NIST `CoolProp` tool used for thermodynamic analysis, a fluid exists as a supercritical liquid or supercritical vapor as long as it remains above the critical temperature. It is then referred to as a liquid or vapor depending on whether it is above or below the critical entropy of the fluid. This NIST convention will be used hereafter throughout discussion.

4.4 Performance Results

The pressurized pumped loop system is able to deliver stable mass fluxes to the test section at the low mass flow rates prescribed for their design. Additionally, a stable pressure differential is maintained between the two sides of the system, where the high-pressure state is maintained between the pump outlet and restriction valves preceding the chiller, and a low-pressure state is maintained everywhere else. Additionally, the facility was able to achieve up to a 300 psi high-pressure ceiling across all test iterations.

Intervals are analyzed after data collection to quantify heat transfer behaviors. These intervals either involve a phase transition from a liquid to a supercritical vapor state or for heat input to the fluid mainly undergoing a two-phase boiling process. The first interval investigated goes through a full change of phase from liquid to supercritical vapor, and is used an the example for the full process of data reduction for the other intervals to follow.

The mass-flow rate of this phase change interval is calculated by the following two methods: via the flow measurements acquired by the volumetric flow meter ($\dot{m}_{flow}$), and via the measurements of heat flux through all the individual fins ($\dot{m}_{flux}$). These calculations come from the primary data source of volumetric flow measurements - from which a mass flow rate is determined from the fluid density - and the thermocouple measurements - from which the local rates of heat transfer through the fins are quantified and also used to determine mass-flow. These data are shown in Fig 4.6.

Using the measured system data, the flow behavior and heat input from each fin can be determined for each of the discrete fluid packets within the test section channel. These can be referenced in Fig 4.7. The fluid flow remains turbulent through the single-phase

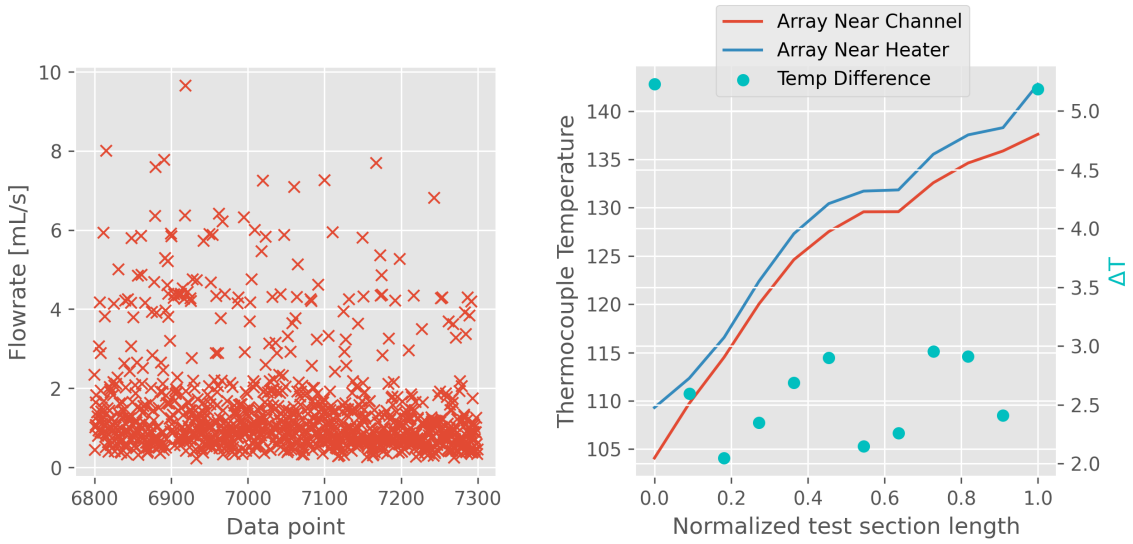

(a) Volumetric flow rate data

(b) Thermocouple measures within fins

Fig. 4.6: Data measures for determining mass-flow for first test interval

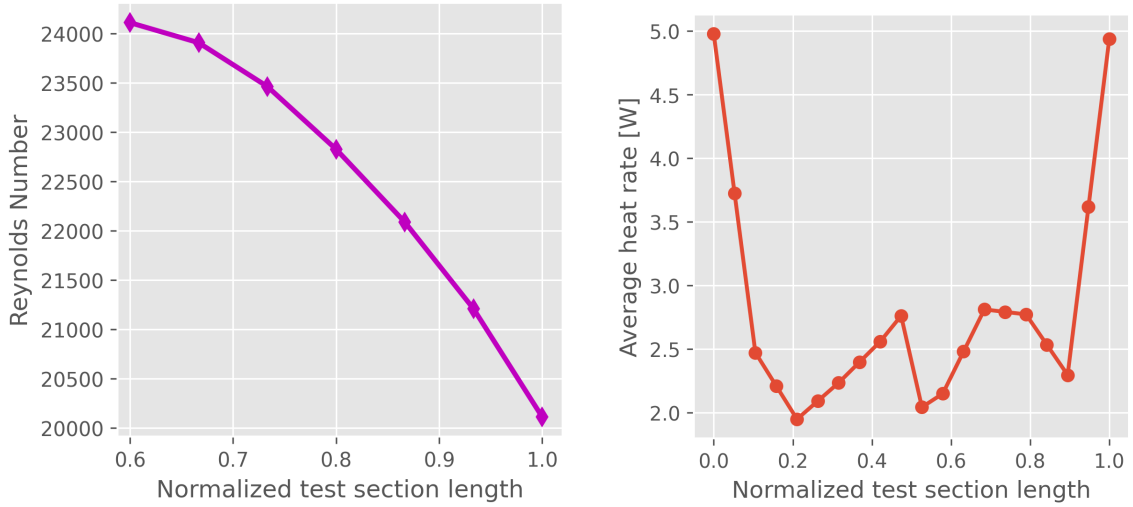

(a) Reynolds number

(b) Fin heat rates

Fig. 4.7: Flow regime and heat input for discrete fluid packets in the channel

state and as it exits the channel, based on the Reynolds number in (a), with the value of the Reynolds number decreasing towards the outlet due to the increasing viscosity of the fluid as it is heated. The heat rates from each fin, shown in (b), are fairly equal throughout the majority of its length, except at the ends where it peaks. It is worth noting that the heat rates shown here are just for a single side of the test section, so the local heat input

from each fin is effectively doubled from these values.

The mass-flow rates calculated for the phase change interval are shown in Table 4.2. The values of the fluid flow rate fall within the low desirable range that the test section was engineered for. Even though the error is significant, it still falls below the allowable threshold. The error is likely due to how low the flow-rate is, causing large consequences from minor perturbations in fluid flow or systematic data capture, which can be seen in the volumetric flow rate data. However, the technique of averaging over a long intervals aids in mitigating the effect of an outlier. Using these mass-flow rates, the wall and fluid temperature are determined, with these results plotted in Fig 4.8.

Table 4.2: Mass flow rates for phase change interval

Parameter	**Value**
$\dot{m}_{flow}$	0.887 [g/s]
$\dot{m}_{flux}$	0.741 [g/s]
Error	16.5%

The temperature curves calculated for the fluid are shown for both mass-flow rates determined in the previous step.

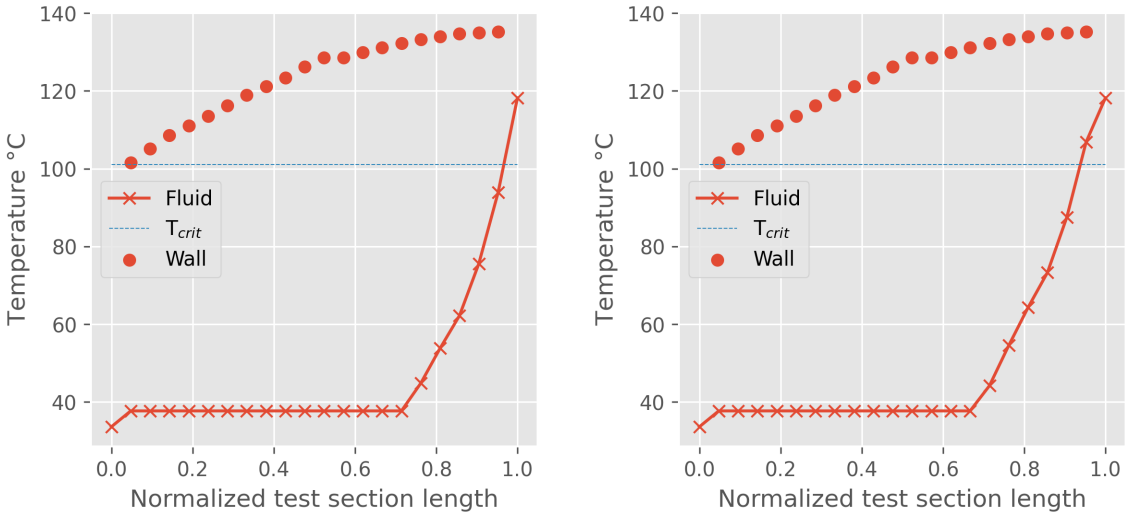

(a) Fluid and wall temperatures via flux

(b) Fluid and wall temperatures via flow

Fig. 4.8: Temperature curves through channel using both mass flow approaches

While the error between mass-flow measures is significant, the overall effect on differences in the fluid temperature curves is minimal, causing the slower stream to heat up faster. Yet, through the method of averaging adjacent bulk fluid temperatures to access thermodynamic properties underneath a specific fin, the effect of the differences is mitigated. Therefore, both approaches provide a sensible way to quantify the addition of heat into the fluid. For the remainder of the test intervals, the flux-based calculation of the mass-flow rate is used for this step.

Based on the fluid temperature curve, four distinct phases are present, considering superheating above the critical temperature of the R134a working fluid. From here, the convective heat transfer coefficients of each discrete fluid packet in the channel can be determined. This is done for both the two-phase heat addition process and the superheating process and shown in Fig 4.9. Additionally, the Nusselt number is calculated during the single phase superheating.

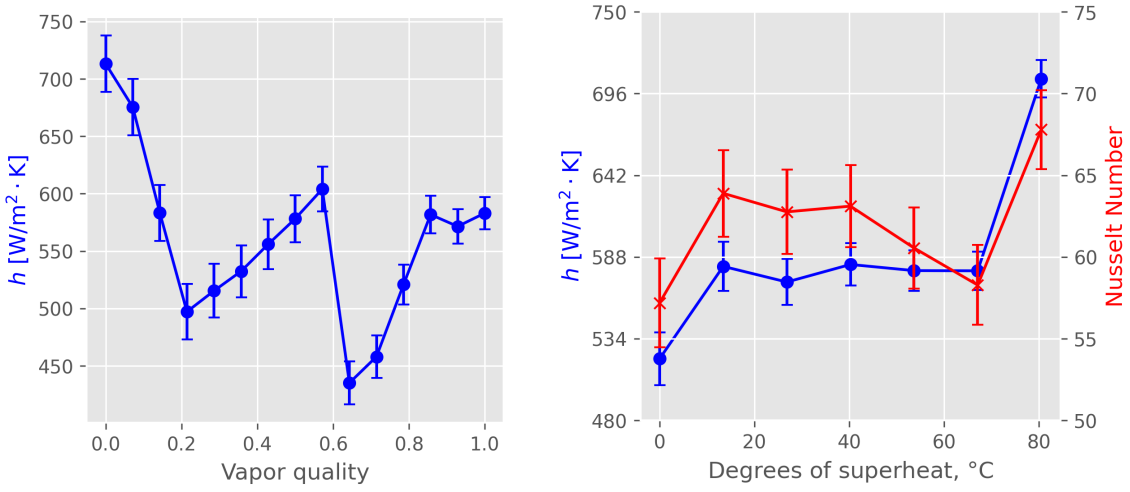

(a) h versus vapor quality

(b) h and Nu versus amount of superheat

Fig. 4.9: Convective heat transfer for two-phase and superheating processes for first interval

The convective heat transfer coefficient of the fluid versus vapor quality during two-phase heating (a) is plotted alongside convective heat transfer and Nusselt number versus the degree of superheat above the fluid's saturation temperature (b). In plot (a), the

convection coefficient peaks at the inlet, mostly likely due to inlet effects from a zero heat influx to peak heat input transition. Some early boiling of the fluid at the inlet may also be at play not easily deduced by a single temperature probe. The coefficient drops quickly, but climbs to its second peak around the center of the two-phase transition. This is likely due to the nucleate boiling phenomenon, which can further describe the drop in heat transfer performance as the fluid nears a fully vapor state where the annular boiling mode dominates. This appears to follow the classic boiling curve. The superheating convective performance in (b) is quite steady, but rises slowly as the fluid and wall temperatures near each other. However, the final packet takes a large jump in performance at the outlet of the test section. While not as large as the inlet, it presents an interesting anomaly. This may be an effect of the large amount of conducting material at the inlet/outlet of the test section acting as a large thermal mass or may be due to other aspects of the component hardware not yet considered.

Next, the Nusselt number calculation for single-phase heat transfer during superheating is further compared to heat transfer correlations from the literature.

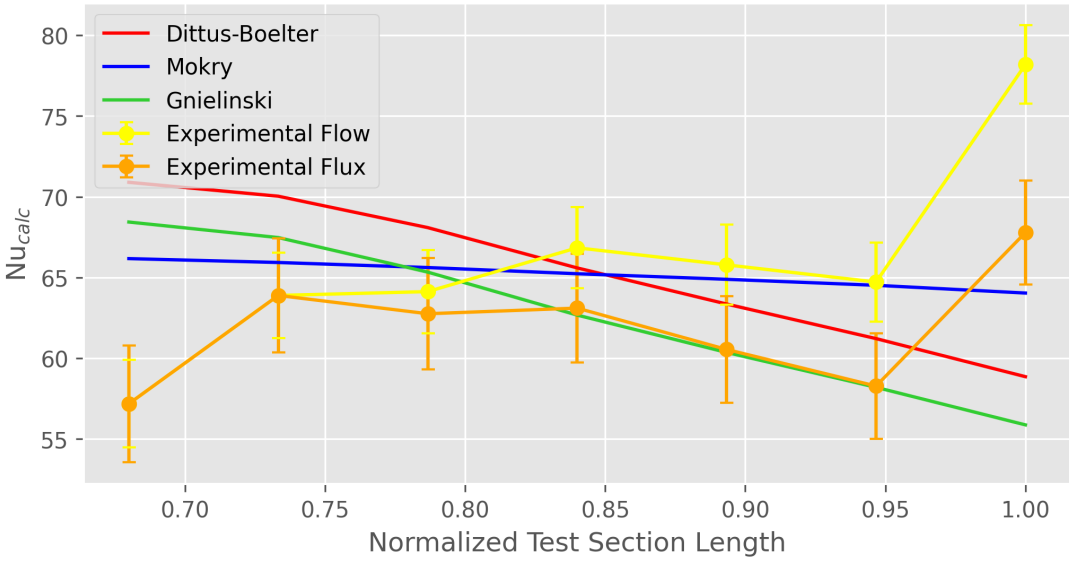

Fig. 4.10: Comparison of Nusselt number from experiment and correlations for superheat phase

The Nusselt number is evaluated from experimental metrics using Eqn 4.2 for both the flux- and flow-based methods along with the chosen heat transfer correlations, and is shown in Fig 4.10. All derivations show that heat transfer performance is greatest at the start of the superheating process as the fluid just exits the two-phase region, with a slow decline of various degrees shown by all of the Nusselt methods. The experimental flux-based results best agree with the Gnielinski correlation, while the other correlations mildly overestimate the performance. On the other hand, the flow-based measurement actually has a lower overall error when compared to the Mokry correlation used. However, the Dittus-Boelter relation better describes the larger magnitude in the downward slope of the experimental flow calculation. This more severe downward trend is likely closer to the reality due to the decreasing turbulence (Fig 4.7(b)) through the latter third of the channel where superheating takes place.

Each of the correlations may theoretically be applicable to this test case as the flow conditions of Reynolds and Prandtl values fall within the relevant range for Dittus-Boelter, Gnielinski ($0.7 < Pr < 120$ and $2{,}500 < Re < 124{,}000$), and for the Mokry correlation. Small deviations in experimental mass-flow do significantly affect how well the experimental calculation of the Nusselt number agree with any individual correlation. To this point, repeated tests with the same heating values and inlet flow conditions will better suggest the correlation with consistent agreement.

A second test interval again undergoes a transition from a liquid to supercritical vapor. The volumetric flow and fin temperature measurements are given in Fig 4.11.

With these data, mass-flow rates are again calculated via two methods for this interval with the results shown in Table 4.3.

Table 4.3: Mass flow rates for second phase change interval

Parameter	**Value**
$\dot{m}_{flow}$	0.818 [g/s]
$\dot{m}_{flux}$	0.856 [g/s]
Error	4.7%

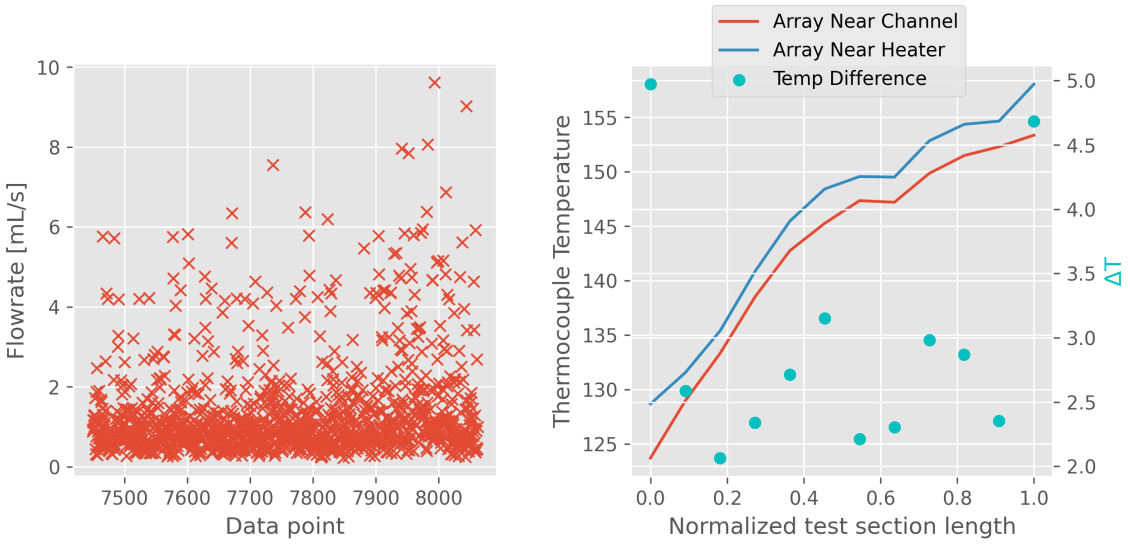

(a) Volumetric flow rate data

(b) Thermocouple measures within fins

Fig. 4.11: Data measures for determining mass-flow for second test interval

In this test case, the resulting error between calculated mass-flows is much lower and below significance, while remaining under a single gram per second.

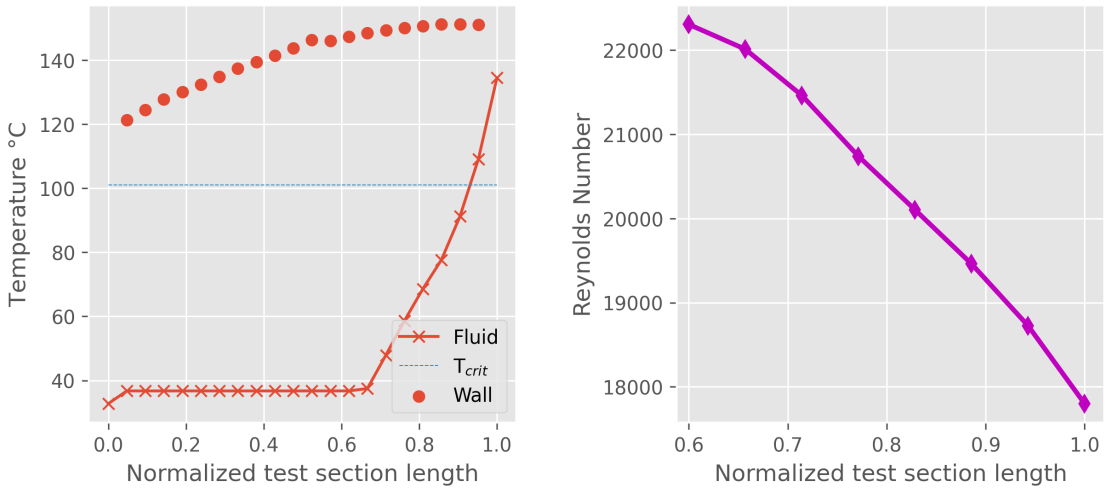

(a) Fluid and wall temperatures

(b) Reynolds number across channel

Fig. 4.12: Flow and temperature measures for second phase change interval

The flow condition across the channel and both fluid and wall temperatures may be referenced by the two subplots in Fig 4.12. The overall length of the two-phase region and

superheating interval are quite similar to the first phase change interval, showing slightly lower turbulence based on the Reynolds number. Similarly to the first interval, the convective heat transfer coefficient is plotted during the two-phase heat, alongside both the convective heat transfer coefficient and the Nusselt number during the superheating process thereafter. These are shown in Fig 4.13.

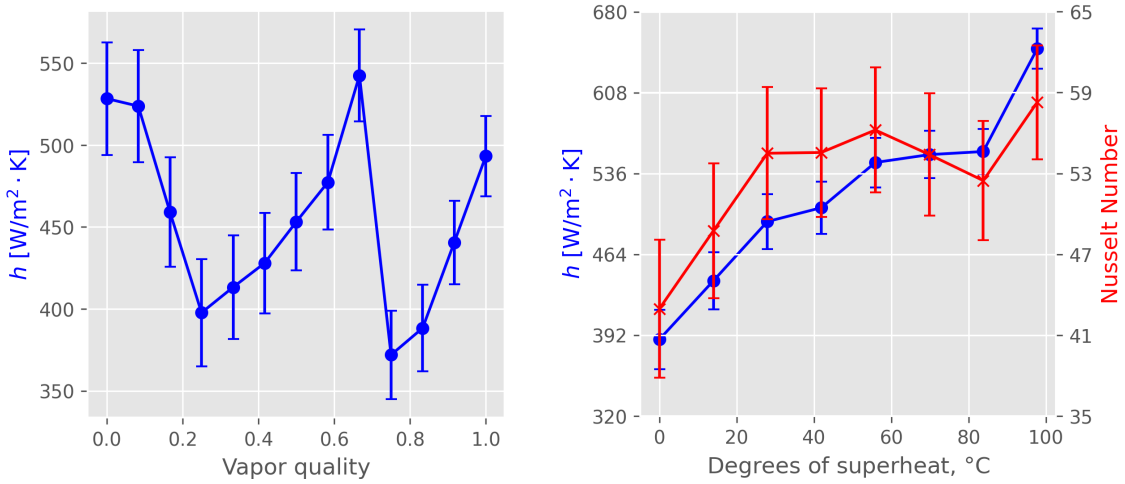

(a) h versus vapor quality

(b) Nu and h versus degrees of superheat

Fig. 4.13: Heat transfer performance during the second phase change interval

The general trend of convective performance during two-phase heating (a) is nearly identical to that of the first interval, but with more attenuated limits on the values. The initial performance through the first half still follows the predicted elevated heat transfer compared to the near fully-vapor state. The Nusselt number shown in (b) is also quite similar to the values calculated in the previous interval. The biggest difference is in the slow rise in convective heat transfer as the fluid becomes more superheated towards the channel outlet. This may be an effect of the rise in the fluid's thermal conductivity and reduction in specific heat as its temperature increases. However, and alike the first interval, the last data point takes an anomalous jump in value that is not clearly explained by the captured data.

Next, the Nusselt number determined using both flux- and flow-based methods are again compared to the same correlations, shown in Fig 4.14

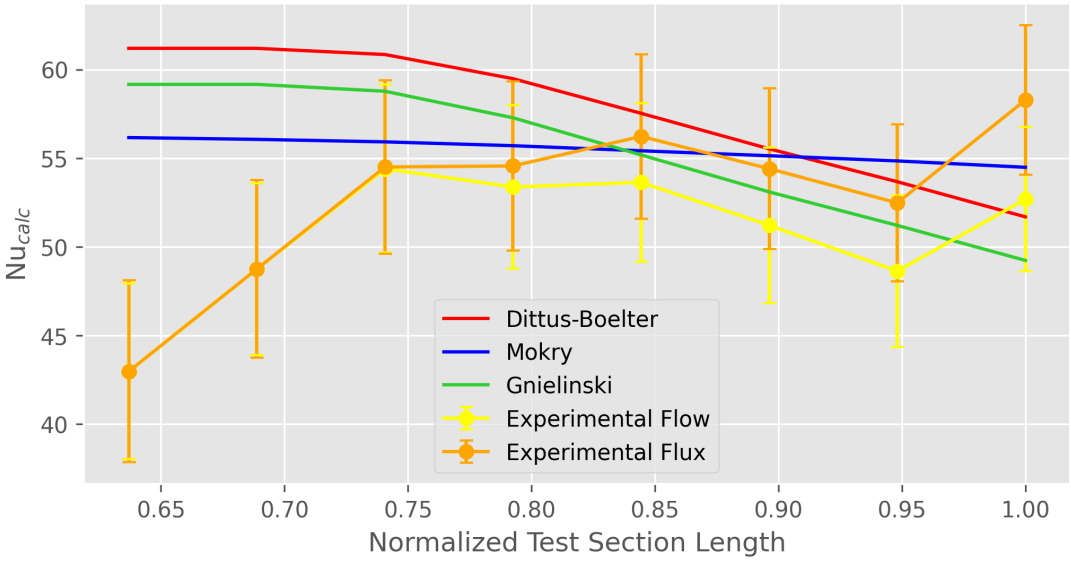

Fig. 4.14: Comparison of Nusselt number from experiment and correlations for superheat phase of second test interval

Once more, the two experimental calculations are quite close and show the same decreasing trend as the fluid flows through the 20% channel which are also indicated by the Dittus-Boelter and Gnielinski correlations. Again, the two experiments agree well with these two correlations in this region, but have flipped in which agrees better due to the flux-based approach possessing a larger mass-flow compared to flow-based. The jump at the outlet is also attenuated to a lower peak compared to the first interval. Similar to the first test, the correlations overestimate heat transfer performance as superheating begins, and the Mokry correlation likely overestimates across the entire length. Yet, this second similar end result to the first interval helps demonstrate a leaning towards reproducibility in test cases.

A third test interval involves heating during a majority two-phase condition during heat addition. The mass-flow rates are again determined using the two methods and shown in Table 4.4.

Table 4.4: Mass flow rates for two-phase interval

Parameter	Value
$\dot{m}_{flow}$	1.821 [g/s]
$\dot{m}_{flux}$	1.866 [g/s]
Error	2.5%

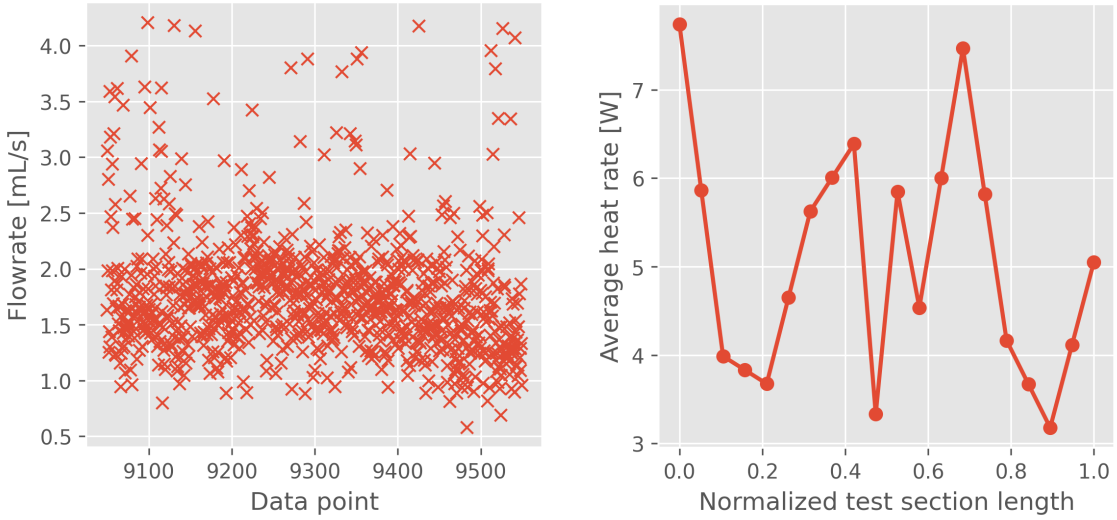

(a) Volumetric flow data

(b) Heat rate across channel

Fig. 4.15: Flow and heat measures for a steady-state two-phase heat addition

The values here agree very well with each other, showing no significant error between and well below the allowable threshold. This is likely due to the elevated flow-rate compared to the first interval and length of the test. The volumetric flow measures reveal less erroneous spikes and a smoother, more consistent measure. Additionally, the heat rate into the channel on average is much larger when compared to the phase change test intervals. These data may be referenced for this interval in Fig 4.15 (a) and (b) respectively.

Similarly, the temperature curves and convective heat transfer coefficients for the discrete fluids packets are calculated and plotted alongside each other in Fig 4.16.

The temperature curves between the wall and the fluid come to a very close pinch near the first third of the channel where convective heat transfer is the greatest, resulting in the high coefficient values. The convective performance is much greater, notably by accommodating a larger mass-flow rate and more substantial two-phase heating across the

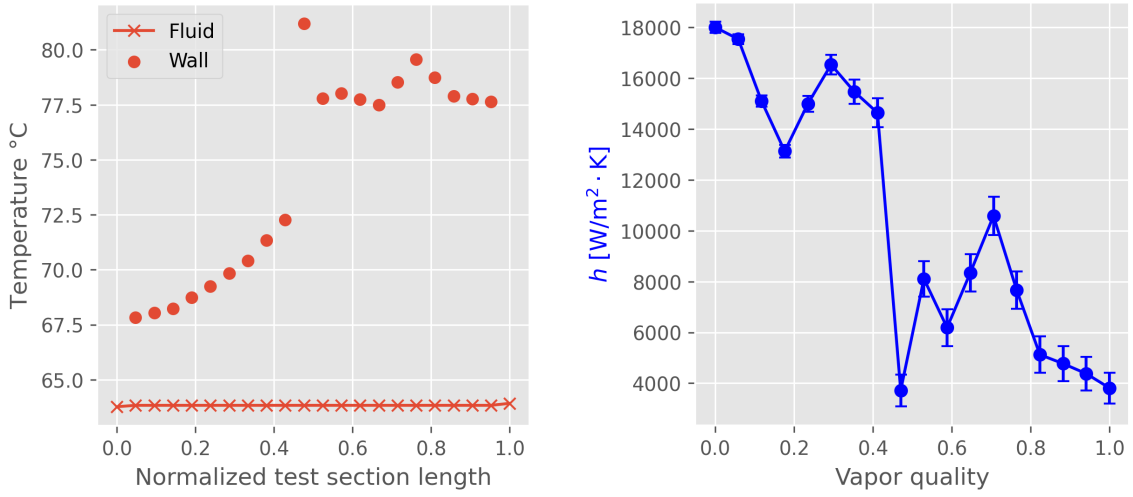

(a) Fluid and wall temperatures

(b) Convective heat transfer

Fig. 4.16: Fluid heat measures for interval three during steady-state two-phase heat addition

channel compared to the first interval. The effect of nucleate boiling is likely at play again, since convective performance difference between the highest point at initial boiling and the lowest is an order of magnitude.

During this two-phase heat input, the best heat transfer performance is measured near the inlet of the test section. The values of performance fall significantly through the latter half of the channel. The uncertainty remains here that a two-phase condition may already be met at the inlet to the channel that could not be accurately captured by the test apparatus.

The experimental heat transfer performance follows expected trends based on a theoretical approach. Still, some care may be taken to improve the measurements collected by the bench-top facility. Fully-utilizing every fin for thermocouple measurements may provide more accurate data compared with the averaging techniques used here. More substantially, uneven pressure perturbations from fluid delivery into the channel may lead to deviations in fluid measures not appropriately alleviated by averaging over a long period. The long interval steady state times were implemented to combat this. Hardware improvement and new components, such as a buffer tank immediately following the pump, may also aid in steadying flow measures. Again, repetition in tested cases of heat input and fluid flow inlet conditions to the test section channel will aid in reducing uncertainties from parts of the

bench-top facility. This will further reduce errors from systematic uncertainties and better align the deviation between the flow- and flux-based metrics calculated for performance.

Additionally, during two-phase heating, comparison to boiling heat transfer coefficients from correlations such as Chen's, Shah's, and Kandlikar's can provide further insight and possible better agreement with experimental measures of convective performance, especially during intervals where quantification of the Nusselt number is not applicable.

4.5 Quantification of Uncertainties

To support the usefulness of the metrics determined in the results, a proper analysis of the uncertainties within the system measurements and calculations must be quantified. For systematic errors from measurement devices, the thermocouples with a tolerance of ± 0.5K which translates to a 0.2% maximum relative uncertainty. The pressure transducers are all rated with a full-scale relative uncertainty of 0.25%. Similarly, the volumetric flow-meter possesses a relative uncertainty of 0.5%. These measures are used both in direct calculations and for indexing other thermodynamics properties by pinning the fluid state at a specific pressure and temperature (or quality when applicable). For thermodynamic calculation purposes, uncertainties are measured by determining the bounds of a calculated property given the range of states it may define, which is referred to as material uncertainties. Random uncertainties are quantified for each variable with a confidence interval of 95% using a student's t-distribution due to the low (1 or 2) repeated number of test cases. From here, a variable's total uncertainty is determined via Eqn 4.16:

$$U_{X_{tot}} = \sqrt{U_{X_r}^2 + U_{X_1}^2 + U_{X_2}^2 \dots U_{X_n}^2}, \tag{4.16}$$

where U_{X_r} is the associated random uncertainty of the variable and each U_{X_i} are the applicable systematic and/or material uncertainties. These then propagate to the final calculations of convective heat transfer and the Nusselt number, which are given respectively by the following data reduction equations:

$$h_i = \frac{k_f \left(T_{h,i} - T_{c,i}\right)}{(T_w - T_{f,b}) d_{TC}} \tag{4.17}$$

and:

$$Nu_i = \frac{k_f D_h \left(T_{h,i} - T_{c,i}\right)}{\lambda (T_w - T_{f,b}) d_{TC}} \tag{4.18}$$

Two methods are utilized in quantifying uncertainty. The Taylor series method for uncertainty analysis is commonplace in quantifying error ranges in experimental data collection and calculations. A less common, yet emerging, mode of quantifying uncertainties is through the Monte Carlo method which uses the statistical distributions of the variables used in the calculation of metrics from experimental data. This method may apply well to this experiment due to the long periods of data collection using devices with relative uncertainties, leading to strong Gaussian distributions of the collected data. The Taylor series method follows the approach of calculating the partial derivative, θ, relative to every variable in the data reduction equation. With all partials and total uncertainties for each variable quantified, the total propagated uncertainty for the calculated metric is:

$$U_{prop}^2 = \sum^{j} \theta_j^2 U_j^2 \tag{4.19}$$

The Monte Carlo method works by randomly sampling from the statistical distribution of each variable used in propagation and calculating the final parameter. This is performed large number of times to determine a final statistical distribution of the final metric. For this study, the variables from a data reduction equation are sampled 10,000 times to generate a roughly Gaussian distribution for the convective heat transfer and Nusselt numbers across the flow channel.

Based on this study's method, 11 total variables were propagated. Both methods are applied to the first test interval and compared. It is shown that the two methods performed nearly identically for the points of maximum uncertainty. The Monte Carlo method tended to take a conservative approach where uncertainties for each local measure had less deviation

between each other due to the higher dependence on the intrinsic statistical behavior of systematic uncertainties. The Taylor series method was more forgiving overall with generally tighter tolerances on final measures.

See the comparison in quantifying uncertainties of the Nusselt number which involved the longest propagation of measured data through different calculations below in Fig 4.17:

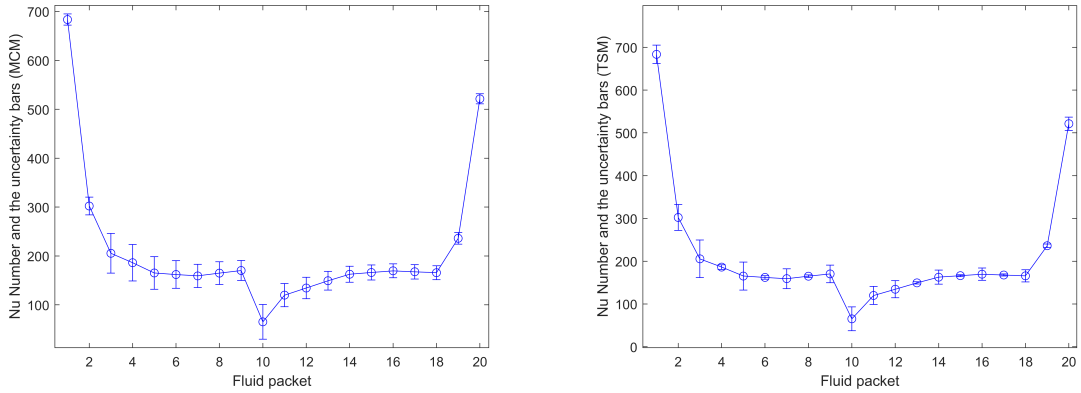

(a) Monte Carlo Method (b) Taylor Series Method

Fig. 4.17: Comparison of two uncertainty methods applied to the first interval Nusselt number calculation

The Monte Carlo method is implemented in final uncertainties to allow for greater tolerance in final measures due to the somewhat anomalous behaviors in the final heat transfer metrics.

CHAPTER 5
CONCLUSIONS

A novel mixed fluid transcritical cycle design for a nuclear small modular reactor is built using `MATLAB/Python`. Through parametric evaluation, a ethanol-CO2 mixture has been shown to provide comparable thermodynamic performance to baseline power cycle designs. Simulation demonstrated the efficacy of pure alcohols as a coolant for the specific power cycle application. However, the lack of significantly superior performance and the the addition of system complexity leaves this design in a state that does not immediately draw further interest. The thermodynamic performance of a mixture did not immediately provide thermodynamic benefits using this cycle design. Yet, it is still unclear as to the viable thermal transport benefits that may be exploited by using a mixture fluid, such as enhancements to two-phase boiling or turbulence effects. The need for physical data when using a non-ideal mixture will likely change the focus of the evaluation to other measures not limited to system output performance. Due to the decoupled nature of the study, a more in depth, coupled simulation may shed light on these benefits in a smaller scale application.

The connection is clearly made based on the modeling of the mixed-fluid transcritical cycle and other experimental works, that a lack of understanding persists for the heat transfer behavior of supercritical fluids. Thus, an experimental setup is developed for the long-term purpose of investigating fluids of interest. A bench-top facility is constructed for providing complete boiling and condensation of a fluid of interest in a pumped loop circuit to evaluate heat transfer performance during heat input. Although the experimental apparatus was not able to achieve a pressure ceiling high enough to evaluate heat transfer performance of a fluid operating at a thermodynamic state at the peak of its vapor dome, phase transitions to a supercritical gas were achieved. It was shown that heat input across a single superheating phase agreed well with established Nusselt correlations, yet no sin-

gle correlation reliably predicted the continuous heat transfer across the entire channel or superheating process. Conversely, a two-phase boiling process consistently demonstrated the best heat transfer performance. Agreement with established heat transfer correlations was best for larger mass-flow rates and lower overall temperature changes, leading to lower errors between end metrics.

Future work with the system has been secured with the modular design of the bench-top apparatus, modular flow channel in the test section for different dimensions or perturbations, and the design and fabrication of a subsequent test section component with higher resilience and fluid-material compatibility. All these parameters allow for handling new facility components and other desired fluids of interest. Small changes to the facility, such as expansion tanks after the pump, a more robust pump controller, and a back-pressure regulator may provide the immediate steps to assuage uncertainties with system measures and attain the pressure ceiling to evaluate heat transfer of fluids existing in their pseudocritical domain.

REFERENCES

[1] D. Bauer, M. Philbrick, and B. Vallario, "The water-energy nexus: Challenges and opportunities," U.S. Department of Energy, Tech. Rep., 2014. [Online]. Available: https://www.energy.gov/articles/water-energy-nexus-challenges-and-opportunities

[2] D. S. Naruka, R. Dwivedi, and P. K. Singh, "Experimental inquisition of heat pipe: performance evaluation for different fluids," *Experimental Heat Transfer*, vol. 33, no. 7, pp. 668–682, 2020. [Online]. Available: https://doi.org/10.1080/08916152.2020.1713254

[3] M. Imran, F. Haglind, M. Asim, and J. Zeb Alvi, "Recent research trends in organic Rankine cycle technology: A bibliometric approach," *Renewable and Sustainable Energy Reviews*, vol. 81, no. December 2016, pp. 552–562, 2018. [Online]. Available: http://dx.doi.org/10.1016/j.rser.2017.08.028

[4] S. Iglesias Garcia, R. Ferreiro Garcia, J. Carbia Carril, and D. Iglesias Garcia, "A review of thermodynamic cycles used in low temperature recovery systems over the last two years," *Renewable and Sustainable Energy Reviews*, vol. 81, no. December 2016, pp. 760–767, 2018. [Online]. Available: http://dx.doi.org/10.1016/j.rser.2017.08.049

[5] M. Holik, M. Živić, Z. Virag, and A. Barac, "Optimization of an organic Rankine cycle constrained by the application of compact heat exchangers," *Energy Conversion and Management*, vol. 188, no. March, pp. 333–345, 2019. [Online]. Available: https://doi.org/10.1016/j.enconman.2019.03.039

[6] T. Hung, "A review of organic Rankine cycles (ORCs) for the recovery of low-grade waste heat," *Fuel and Energy Abstracts*, vol. 39, no. 2, pp. 151 –, 1998. [Online]. Available: http://www.sciencedirect.com/science/article/pii/S0140670198978948

[7] T. Tartière and M. Astolfi, "A World Overview of the Organic Rankine Cycle Market," *Energy Procedia*, vol. 129, pp. 2–9, 2017. [Online]. Available: http://dx.doi.org/10.1016/j.egypro.2017.09.159

[8] H. Chen, D. Y. Goswami, M. M. Rahman, and E. K. Stefanakos, "A supercritical Rankine cycle using zeotropic mixture working fluids for the conversion of low-grade heat into power," *Energy*, vol. 36, no. 1, pp. 549–555, 2011. [Online]. Available: http://dx.doi.org/10.1016/j.energy.2010.10.006

[9] S. Karellas, A. Schuster, and A. D. Leontaritis, "Influence of supercritical ORC parameters on plate heat exchanger design," *Applied Thermal Engineering*, vol. 33-34, no. 1, pp. 70–76, 2012. [Online]. Available: http://dx.doi.org/10.1016/j.applthermaleng.2011.09.013

[10] V. L. Le, M. Feidt, A. Kheiri, and S. Pelloux-Prayer, "Performance optimization of low-temperature power generation by supercritical ORCs (organic Rankine cycles) using low GWP (global warming potential) working fluids," *Energy*, vol. 67, pp. 513–526, 2014. [Online]. Available: http://dx.doi.org/10.1016/j.energy.2013.12.027

[11] X. Wang, E. K. Levy, C. Pan, C. E. Romero, A. Banerjee, C. Rubio-Maya, and L. Pan, "Working Fluid Selection for Organic Rankine Cycle Power Generation Using Hot Produced Supercritical CO2 From a Geothermal Reservoir," *Applied Thermal Engineering*, 2019. [Online]. Available: https://doi.org/10.1016/j.applthermaleng.2018.12.112

[12] I. H. Bell, J. Wronski, S. Quoilin, and V. Lemort, "Pure and pseudo-pure fluid thermophysical property evaluation and the open-source thermophysical property library coolprop," *Industrial & Engineering Chemistry Research*, vol. 53, no. 6, pp. 2498–2508, 2014. [Online]. Available: http://pubs.acs.org/doi/abs/10.1021/ie4033999

[13] C. Invernizzi, *Closed Power Cycles. Thermodynamic Fundamentals and Applications*, 01 2013, vol. 11.

[14] S. Karellas and A. Schuster, "Supercritical fluid parameters in organic rankine cycle applications," *International Journal of Thermodynamics*, vol. 11, no. 3, pp. 101–108, 2008. [Online]. Available: https://dergipark.org.tr/en/download/article-file/65731

[15] P. Colonna, E. Casati, C. Trapp, T. Mathijssen, J. Larjola, T. Turunen-Saaresti, and A. Uusitalo, "Organic Rankine Cycle Power Systems: From the Concept to Current Technology, Applications, and an Outlook to the Future," *Journal of Engineering for Gas Turbines and Power*, vol. 137, no. 10, p. 100801, 2015. [Online]. Available: https://doi.org/10.1115/1.4029884

[16] J. Bao and L. Zhao, "A review of working fluid and expander selections for organic Rankine cycle," *Renewable and Sustainable Energy Reviews*, vol. 24, pp. 325–342, 2013. [Online]. Available: http://dx.doi.org/10.1016/j.rser.2013.03.040

[17] S. A. Jajja, K. R. Zada, and B. M. Fronk, "Experimental investigation of supercritical carbon dioxide in horizontal microchannels with non-uniform heat flux boundary conditions," *International Journal of Heat and Mass Transfer*, vol. 130, pp. 304–319, 2019. [Online]. Available: https://doi.org/10.1016/j.ijheatmasstransfer.2018.10.027

[18] J. Ringler, M. Seifert, V. Guyotot, and W. Hübner, "Rankine cycle for waste heat recovery of IC engines," *SAE International Journal of Engines*, vol. 2, no. 1, pp. 67–76, 2009. [Online]. Available: https://www.jstor.org/stable/10.2307/26308377

[19] Z. Mat Nawi, S. K. Kamarudin, S. R. Sheikh Abdullah, and S. S. Lam, "The potential of exhaust waste heat recovery (WHR) from marine diesel engines via organic rankine cycle," *Energy*, vol. 166, pp. 17–31, 2019. [Online]. Available: https://doi.org/10.1016/j.energy.2018.10.064

[20] M. E. Mondejar, J. G. Andreasen, L. Pierobon, U. Larsen, M. Thern, and F. Haglind, "A review of the use of organic Rankine cycle power systems for maritime applications," *Renewable and Sustainable Energy Reviews*, vol. 91, no. April 2017, pp. 126–151, 2018. [Online]. Available: https://doi.org/10.1016/j.rser.2018.03.074

[21] S. Lecompte, H. Huisseune, M. Van Den Broek, B. Vanslambrouck, and M. De Paepe, "Review of organic Rankine cycle (ORC) architectures for waste heat recovery,"

Renewable and Sustainable Energy Reviews, vol. 47, pp. 448–461, 2015. [Online]. Available: http://dx.doi.org/10.1016/j.rser.2015.03.089

[22] J. Li, Q. Liu, Z. Ge, Y. Duan, and Z. Yang, "Thermodynamic performance analyses and optimization of subcritical and transcritical organic Rankine cycles using R1234ze(E) for 100–200 °C heat sources," *Energy Conversion and Management*, vol. 149, pp. 140–154, 2017. [Online]. Available: http://dx.doi.org/10.1016/j.enconman.2017.06.060

[23] H. Wang and S. Kissick, "Phase report: Power cycle optimization for small modular reactor by nuscale power," December 2017.

[24] S. Kissick, "Power cycle selection and optimization for small modular reactor," Master's thesis, Oregon State University, June 2018.

[25] C. Li, G. Kosmadakis, D. Manolakos, E. Stefanakos, G. Papadakis, and D. Y. Goswami, "Performance investigation of concentrating solar collectors coupled with a transcritical organic Rankine cycle for power and seawater desalination co-generation," *Desalination*, vol. 318, pp. 107–117, 2013. [Online]. Available: https://doi.org/10.1016/j.desal.2013.03.026

[26] C. Vetter, H. J. Wiemer, and D. Kuhn, "Comparison of sub- and supercritical Organic Rankine Cycles for power generation from low-temperature/low-enthalpy geothermal wells, considering specific net power output and efficiency," *Applied Thermal Engineering*, vol. 51, no. 1-2, pp. 871–879, 2013. [Online]. Available: http://dx.doi.org/10.1016/j.applthermaleng.2012.10.042

[27] D. Wang, X. Dai, R. Tian, and L. Shi, "Experimental investigation of the heat transfer of supercritical R134a in a horizontal micro-fin tube," *International Journal of Thermal Sciences*, vol. 138, no. August 2018, pp. 536–549, 2019. [Online]. Available: https://doi.org/10.1016/j.ijthermalsci.2019.01.013

[28] P. X. Jiang, C. R. Zhao, and B. Liu, "Flow and heat transfer characteristics of r22 and ethanol at supercritical pressures," *Journal of Supercritical Fluids*, vol. 70, pp. 75–89, 2012. [Online]. Available: http://dx.doi.org/10.1016/j.supflu.2012.06.011

[29] B. F. Tchanche, G. Lambrinos, A. Frangoudakis, and G. Papadakis, "Low-grade heat conversion into power using organic Rankine cycles - A review of various applications," *Renewable and Sustainable Energy Reviews*, vol. 15, no. 8, pp. 3963–3979, 2011. [Online]. Available: http://dx.doi.org/10.1016/j.rser.2011.07.024

[30] G. Angelino and P. Colonna Di Paliano, "Multicomponent working fluids for organic Rankine cycles (ORCs)," *Energy*, vol. 23, no. 6, pp. 449–463, 1998. [Online]. Available: https://doi.org/10.1016/S0360-5442(98)00009-7

[31] D. Maraver, J. Royo, V. Lemort, and S. Quoilin, "Systematic optimization of subcritical and transcritical organic Rankine cycles (ORCs) constrained by technical parameters in multiple applications," *Applied Energy*, vol. 117, pp. 11–29, 2014. [Online]. Available: http://dx.doi.org/10.1016/j.apenergy.2013.11.076

[32] A. Schuster, S. Karellas, and R. Aumann, "Efficiency optimization potential in supercritical Organic Rankine Cycles," *Energy*, vol. 35, no. 2, pp. 1033–1039, 2010. [Online]. Available: http://dx.doi.org/10.1016/j.energy.2009.06.019

[33] C. Pumaneratkul, H. Yamasaki, H. Yamaguchi, S. Kitamura, and Y. Sako, "Supercritical CO2 Rankine Cycle System with Low-Temperature Geothermal Heat Pipe," *Energy Procedia*, vol. 105, pp. 1029–1036, 2017. [Online]. Available: http://dx.doi.org/10.1016/j.egypro.2017.03.448

[34] Z. Shengjun, W. Huaixin, and G. Tao, "Performance comparison and parametric optimization of subcritical Organic Rankine Cycle (ORC) and transcritical power cycle system for low-temperature geothermal power generation," *Applied Energy*, vol. 88, no. 8, pp. 2740–2754, 2011. [Online]. Available: http://dx.doi.org/10.1016/j.apenergy.2011.02.034

[35] F. Sun, Y. Li, O. Manca, and G. Xie, "An evaluation on the laminar effect of buoyancy-driven supercritical hydrocarbon fuel flow and heat transfer characteristics," *International Journal of Heat and Mass Transfer*, vol. 142, p. 118414, 2019. [Online]. Available: https://doi.org/10.1016/j.ijheatmasstransfer.2019.07.064

[36] "How the nuscale module works," 2021. [Online]. Available: https://www.nuscalepower.com/technology/technology-overview

[37] "Introduction to Non-ideal Solutions," Sep 2020, [Accessed 2021-11-17]. [Online]. Available: https://chem.libretexts.org/@go/page/74123

[38] D. Wang, R. Tian, Y. Zhang, L. L. Li, Y. Ma, L. Shi, and H. Li, "Heat transfer investigation of supercritical R134a for trans-critical organic Rankine cycle system," *Energy*, vol. 169, pp. 542–557, 2019. [Online]. Available: https://doi.org/10.1016/j.energy.2018.12.034

[39] J. H. Song, H. Y. Kim, H. Kim, and Y. Y. Bae, "Heat transfer characteristics of a supercritical fluid flow in a vertical pipe," *Journal of Supercritical Fluids*, vol. 44, no. 2, pp. 164–171, 2008. [Online]. Available: https://doi.org/10.1016/j.supflu.2007.11.013

[40] L. Chai and S. A. Tassou, "Numerical study of the thermohydraulic performance of printed circuit heat exchangers for supercritical CO 2 Brayton cycle applications," *Energy Procedia*, vol. 161, pp. 480–488, 2019. [Online]. Available: https://doi.org/10.1016/j.egypro.2019.02.066

[41] L. R. Thippeswamy and A. Kumar Yadav, "Heat transfer enhancement using CO2 in a natural circulation loop," *Scientific Reports*, vol. 10, no. 1, pp. 1–10, 2020. [Online]. Available: https://doi.org/10.1038/s41598-020-58432-6

[42] D. Ingersoll, Z. Houghton, R. Snuggerud, J. Gaston, and M. Empey, "Integrating nuclear and renewables," *Nuclear Engineering International*, vol. 61, pp. 37–39, 01 2016.

[43] T. Benson, "Compressor thermodynamics." [Online]. Available: https://www.grc.nasa.gov/www/k-12/VirtualAero/BottleRocket/airplane/compth.html

[44] M. Décultot, A. Ledoux, M. C. Fournier-Salaün, and L. Estel, "Solubility of CO2 in methanol, ethanol, 1,2-propanediol and glycerol from 283.15.K to 373.15.K and up to 6.0.MPa," *Journal of Chemical Thermodynamics*, vol. 138, pp. 67–77, 2019. [Online]. Available: https://doi.org/10.1016/j.jct.2019.05.003

[45] X. Nie, Z. Du, L. Zhao, S. Deng, and Y. Zhang, "Molecular dynamics study on transport properties of supercritical working fluids: Literature review and case study," *Applied Energy*, vol. 250, no. January, pp. 63–80, 2019. [Online]. Available: https://doi.org/10.1016/j.apenergy.2019.04.156

[46] H. Pu, S. Li, M. Dong, S. Jiao, Y. Wang, and Y. Shang, "Convective heat transfer and flow resistance characteristics of supercritical pressure hydrocarbon fuel in a horizontal rectangular mini-channel," *Experimental Thermal and Fluid Science*, vol. 108, no. March, pp. 39–53, 2019. [Online]. Available: https://doi.org/10.1016/j.expthermflusci.2019.06.002

[47] E. Wang, Z. Yu, H. Zhang, and F. Yang, "A regenerative supercritical-subcritical dual-loop organic Rankine cycle system for energy recovery from the waste heat of internal combustion engines," *Applied Energy*, vol. 190, pp. 574–590, 2017. [Online]. Available: http://dx.doi.org/10.1016/j.apenergy.2016.12.122

[48] D. A. Kromer, A. J. Huning, and S. Garimella, "I2S-LWR microchannel heat exchanger design and experimental validation," *Annals of Nuclear Energy*, 2018. [Online]. Available: https://doi.org/10.1016/j.anucene.2017.08.043

APPENDICES

APPENDIX A

ADDITIONAL FIGURES AND TABLES

A.1 Figures

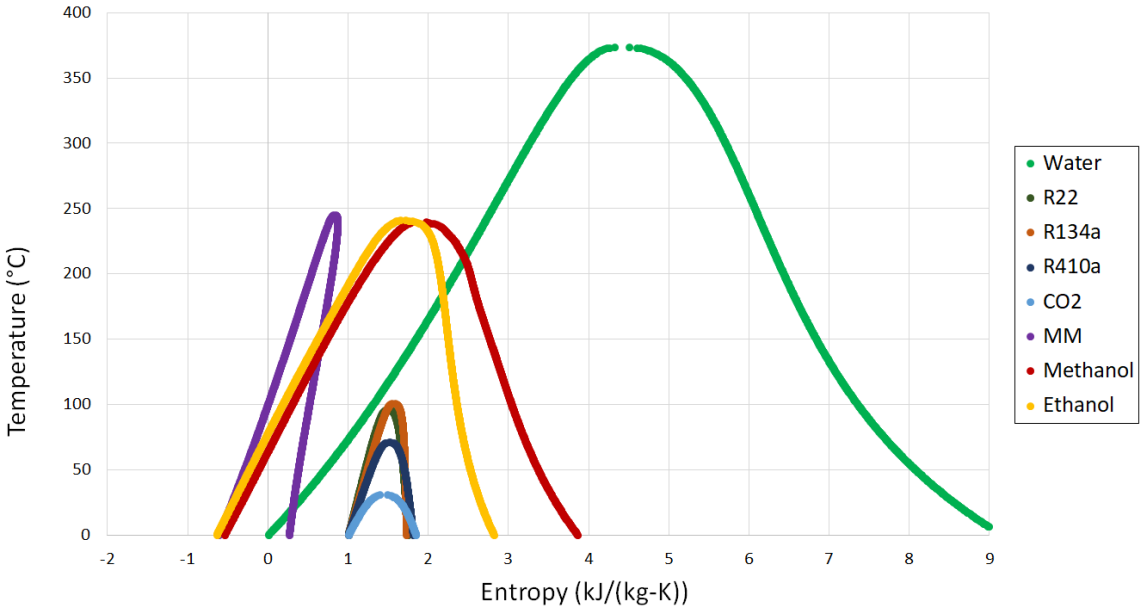

Fig. A.1: T-s diagram showing the vapor dome of common fluids

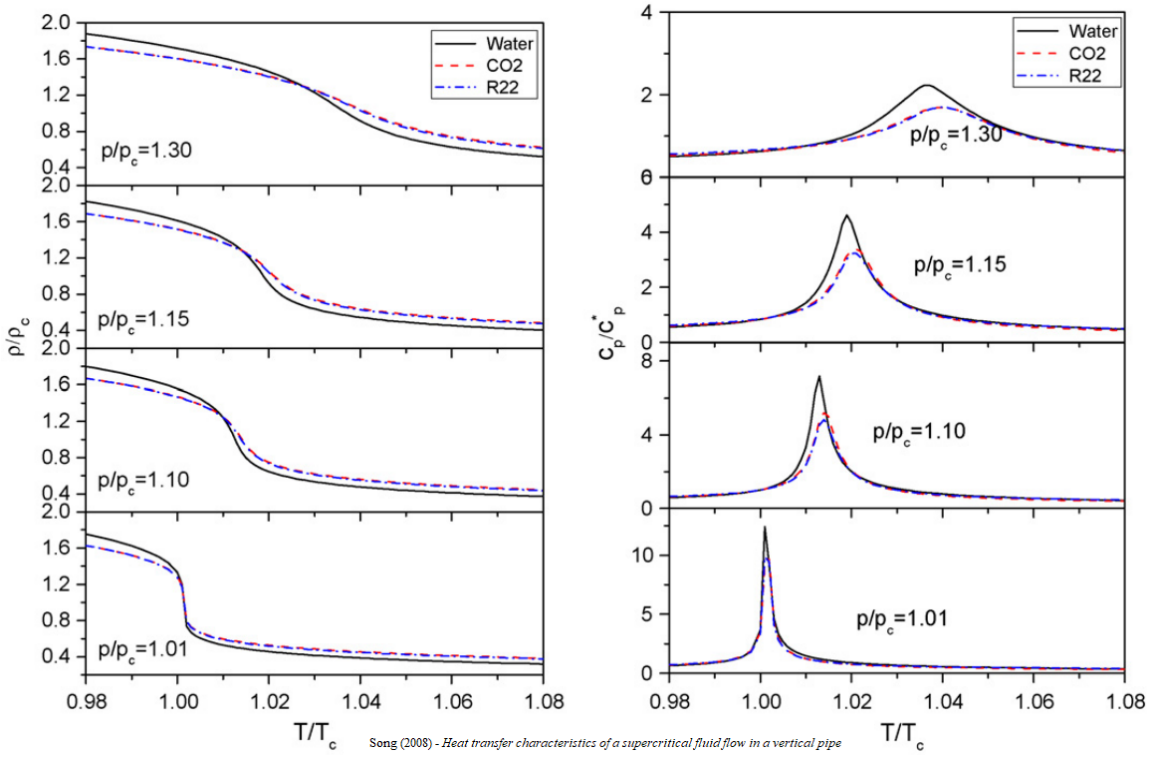

Fig. A.2: Thermo-physical properties for some fluids near critical parameters

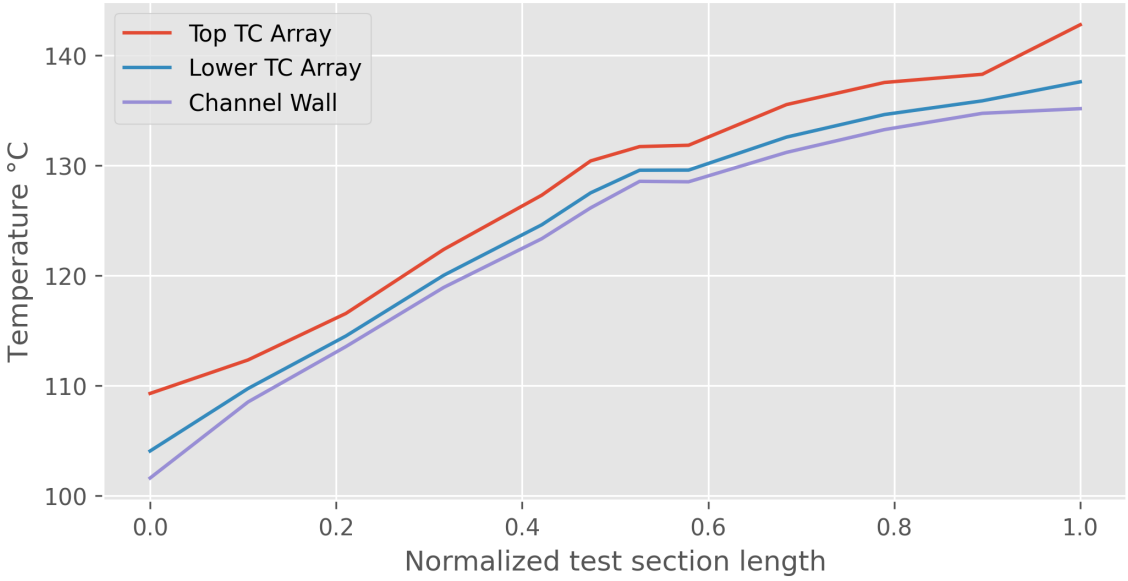

Fig. A.3: Temperatures of both thermocouple arrays and the projected channel wall via 1D conduction

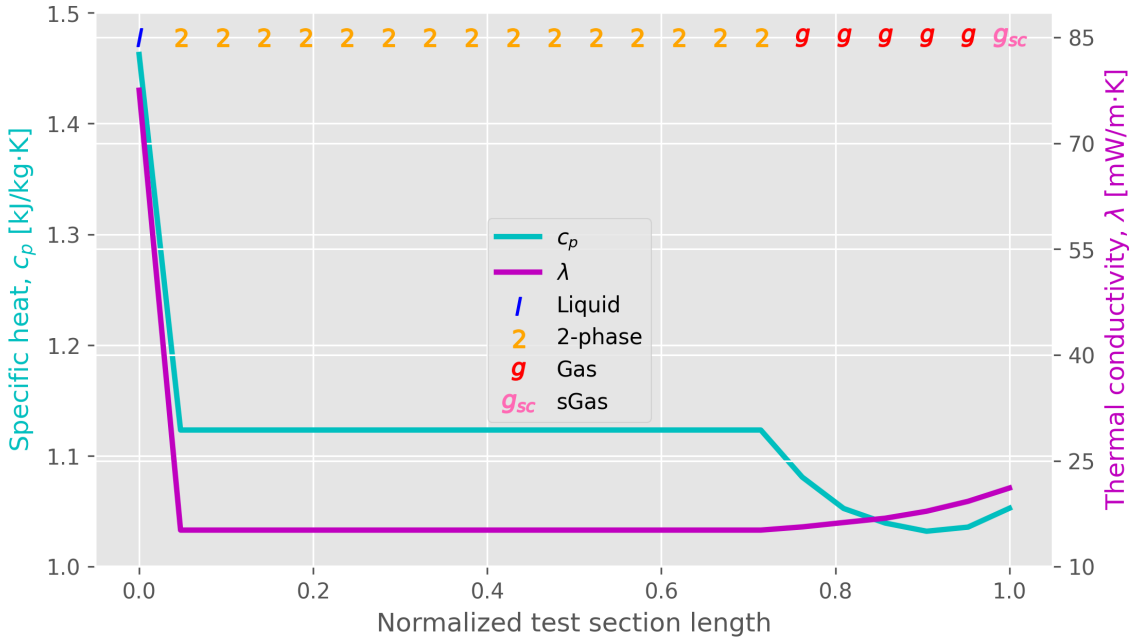

Fig. A.4: Example of local thermodynamic properties/phases for liquid to sc-gas transition

A.2 Tables

Table A.1: Critical parameters, latent heat of vaporization, and dryness of organic fluids

Compound	T_c **[°C]**	P_c **[bar]**	$\Delta_{vap}H^\circ$ **[kJ/kg]**	ξ
Nitrogen	-147	34.0	-	Wet
Carbon Dioxide	31.1	73.9	379.5	Wet
R410a	72.8	49.0	271.7	Wet
R22	96.0	49.8	231.3	Wet
R134a	101	40.6	215.6	Isen.
Methanol	240	81.0	1195	Wet
Ethanol	241	63.0	920.4	Wet
MM	245.5	19.3	227.2	Dry
RP-3	372	23.9	-	-
Water	374	221	2256	Wet

**Note: T_c, P_c, $\Delta_{vap}H^\circ$ data taken at 300K

Table A.2: Collected bulk fluid Nusselt number correlations

Author	**Equation**	**Variable Determination**
Dittus-Boelter (1930)	$Nu_b = 0.023Re_b^{0.8}Pr_b^n$	$n = 0.3$ for cooling $n = 0.4$ for heating
Gnielinski (1976)	$Nu = \frac{(f/8)(Re-1000)Pr}{1+12.7(f/8)^{0.5}(Pr^{2/3}-1)}$	For smooth tubes: $f = (0.790ln(Re) - 1.64)^{-2}$ $10^4 < Re < 10^6$
Jackson and Hall (1979)	$Nu_b = 0.0183Re_b^{0.82}\bar{P}r^{0.5}(\frac{\rho_w}{\rho_b})^{0.3}(\frac{\bar{c}_p}{c_{pb}})^n$	$\bar{c}_p = (\int_{T_w}^{T_b} c_p dT)/(T_b - T_w)$ $n = 0.4$ for $T_b < T_w < T_{pc}$ and $1.2T_{pc} < T_b < T_w$ $n = 0.4 + 0.2[(T_w/T_{pc}) - 1)]$ for $T_b < T_{pc} < T_w$ $n = 0.4 + 0.2[(T_w/T_{pc}) - 1][1 - 5(T_b/T_{pc} - 1)]$ for $T_{pc} < T_b < 1.2T_{pc}$ and $T_b < T_w$
Petukhov (1983)	$Nu_b = \frac{(f/8)Re_b\bar{P}r_b}{1+900/Re_b+12.7\sqrt{f/8}(\bar{P}r_b^{2/3}-1)}$	$f = f_0(\rho_w/\rho_b)^{0.4}(\mu_w/\mu_b)^{0.2}$ $f_0 = (1.82log_{10}(Re_b) - 1.64)^{-2}$
Mokry (2010)	$Nu_b = 0.0345Re_b^{0.77}\bar{P}r^{0.17}(\frac{\rho_w}{\rho_b})^{0.47}$	

APPENDIX B

SOFTWARE

B.1 Python Scripts

Algorithm B.1: Libraries called

```
!pip install coolprop

import CoolProp as CP
import CoolProp.CoolProp as CPCP
import numpy as np
import pandas as pd
import matplotlib.pyplot as plt
```

Algorithm B.2: System specification parameters

```
''' Fluid Parameters '''
fluid = 'R134a'                    # String literal recognized by CoolProp

''' Test Section/Heater Parameters'''
q_dot_heater  = 325 * 2            # Heat input from 1 cartridge heater [W]
Cu_L          = 0.1                # Copper block geometry
Cu_h          = 0.038
Cu_w          = 0.019
Cu_vol        = Cu_L * Cu_h * Cu_w # Volume of copper spreader block [m^3]
Cu_T          = 250 + 273.15       # Held temperature of copper blocks
Cu_k          = 386                # [W/(m-K)] (engineersedge.com)
Al_k          = 167                # Al thermal conductivity [W/(m-K)]
SS_k          = 16.3               # 316 SS thermal conductivity [W/(m-K)]
air_k         = 0.02624            # (engineeringtoolbox.com)
paste_k       = 31.4               # Thermal paste conductivity
fin_h         = 0.015              # Fin geometry (on test section)
fin_w         = 0.019
```

```
fin_th          = 0.003
fin_th_end      = 0.0055            # Thickness of the two end fins
fin_sep         = 0.002             # Separation between fins
fin_num         = 20
testsec_th      = 0.0066            # Thickness of sandwiched plates
chan_L          = 0.17145           # Channel geometry (in the test section)
chan_w          = 0.005
chan_h          = 0.001

fin_Ac          = fin_w * fin_th
chan_Ac         = chan_w * chan_h
chan_As         = (chan_w*chan_L + chan_h*chan_L + chan_w*chan_h)*2
chan_V          = chan_w*chan_h*chan_L
chan_P          = 2*(chan_w + chan_h)
dHydr           = chan_Ac/chan_P
LoverD          = chan_L/dHydr
```

Algorithm B.3: Custom Functions

```
''' Converts a value assumed to a be pressure in psi to another unit. Takes
    the string of the desired unit in first arg, the value to convert second '''
def psi2(val, conversion):
    val = float(val)
    if conversion in ('MPa', 'mpa', 'megapascals', 'Megapascals', 'MPA'):
        return val*0.00689475729
    elif conversion in ('bar', 'Bar', 'BAR'):
        return val*0.0689475729
    elif conversion in ('Pa', 'pa', 'PA', 'Pascals', 'pascals', 'Pascal', 'pascal'):
        return val*6894.75729
    elif conversion in ('kPa', 'kpa' 'kilopascals', 'Kilopascals', 'KPA'):
        return val*6.89475729
    elif conversion in ('atm', 'ATM', 'Atmospheres', 'atmospheres'):
        return val*0.0680459639
    elif conversion in ('torr', 'Torr', 'TORR', 'mmHg', 'MMHG', 'MMHg'):
        return val*51.7149326
    elif conversion in ('inH2O', 'inh2o', 'INH20', 'inchH2O', 'inchesH2O'):
```

```
18          return val*27.6704523
19      elif conversion in ('ftH20', 'FTH20', 'feetH20', 'FeetH20', 'FEETH20'):
20          return val*27.6704523/12
21      else:
22          print('Error trying to convert a psi value')
23          print('I cannot convert that thing to the other thing...')
24
25  class convThis:
26      def __init__(self, val, unit):
27          self.val  = val
28          self.unit = unit
29      def help():
30          print('Use this class by assigning a variable to call it with the value',
31          'and the current unit the value is in as a string in the 1st and 2nd',
32          'arguements respectively. Then call the conversion function as ',
33          '"to_(unit)(). For example:', sep='\n')
34          print('\n')
35          print('myVal = convThis(14.7, "psi")')
36          print('inATM = myVal.to_atm()')
37          print('inATM = 1.0002756693300001')
38          print('\n')
39          print('or')
40          print('\n')
41          print('myVal = convThis(101325, "Pa")')
42          print('inBAR = myVal.to_bar()')
43          print('inBAR = 1.01325')
44      def to_psi(self):
45          if self.unit in ['psi', 'PSI']:
46              return self.val*1
47          elif self.unit in ['mpa', 'MPa', 'MPA']:
48              return self.val*145.037738
49          elif self.unit in ['bar', 'Bar', 'BAR']:
50              return self.val*14.5037738
51          elif self.unit in ['kpa', 'kPa', 'KPA']:
52              return self.val*0.145037738
```

```
53          elif self.unit in ['pa', 'Pa', 'PA']:
54              return self.val*0.000145037738
55          elif self.unit in ['atm', 'ATM', 'atmospheres']:
56              return self.val*14.6959488
57          elif self.unit in ['torr', 'Torr', 'TORR', 'mmHg', 'MMHG']:
58              return self.val*0.0193367747
59          elif self.unit in ['inH2O', 'inh2o', 'INH2O', 'inchH2O']:
60              return self.val*0.0361396333
61          elif self.unit == 'inHg' or self.unit == 'INHG':
62              return self.val*0.49109778
63          else:
64              print('Error when trying to convert something to psi')
65      def to_MPa(self):
66          if self.unit in ['psi', 'PSI']:
67              return self.val*0.00689475729
68          elif self.unit in ['mpa', 'MPa', 'MPA']:
69              return self.val*1
70          elif self.unit in ['bar', 'Bar', 'BAR']:
71              return self.val*0.1
72          elif self.unit in ['kpa', 'kPa', 'KPA']:
73              return self.val*0.001
74          elif self.unit in ['pa', 'Pa', 'PA']:
75              return self.val*0.000001
76          elif self.unit in ['atm', 'ATM', 'atmospheres']:
77              return self.val*0.101325
78          elif self.unit in ['torr', 'Torr', 'TORR', 'mmHg', 'MMHG']:
79              return self.val*0.000133322368
80          elif self.unit in ['inH2O', 'inh2o', 'INH2O', 'inchH2O']:
81              return self.val*0.000249174
82          else:
83              print('Error when trying to convert something to MPa')
84      def to_bar(self):
85          if self.unit in ['psi', 'PSI']:
86              return self.val*0.0689475729
87          elif self.unit in ['mpa', 'MPa', 'MPA']:
```

```
88              return self.val*10
89          elif self.unit in ['bar', 'Bar', 'BAR']:
90              return self.val*1
91          elif self.unit in ['kpa', 'kPa', 'KPA']:
92              return self.val*0.01
93          elif self.unit in ['pa', 'Pa', 'PA']:
94              return self.val*0.00001
95          elif self.unit in ['atm', 'ATM', 'atmospheres']:
96              return self.val*1.01325
97          elif self.unit in ['torr', 'Torr', 'TORR', 'mmHg', 'MMHG']:
98              return self.val*0.00133322368
99          elif self.unit in ['inH2O', 'inh2o', 'INH2O', 'inchH2O']:
100             return self.val*0.00249174
101         else:
102             print('Error when trying to convert something to bar')
103     def to_kPa(self):
104         if self.unit in ['psi', 'PSI']:
105             return self.val*6.89475729
106         elif self.unit in ['mpa', 'MPa', 'MPA']:
107             return self.val*1000
108         elif self.unit in ['bar', 'Bar', 'BAR']:
109             return self.val*100
110         elif self.unit in ['kpa', 'kPa', 'KPA']:
111             return self.val*1
112         elif self.unit in ['pa', 'Pa', 'PA']:
113             return self.val*0.001
114         elif self.unit in ['atm', 'ATM', 'atmospheres']:
115             return self.val*101.325
116         elif self.unit in ['torr', 'Torr', 'TORR', 'mmHg', 'MMHG']:
117             return self.val*0.133322368
118         elif self.unit in ['inH2O', 'inh2o', 'INH2O', 'inchH2O']:
119             return self.val*0.24917400
120         else:
121             print('Error when trying to convert something to kPa')
122     def to_Pa(self):
```

```
123         if self.unit in ['psi', 'PSI']:
124             return self.val*6894.75729
125         elif self.unit in ['mpa', 'MPa', 'MPA']:
126             return self.val*1000000
127         elif self.unit in ['bar', 'Bar', 'BAR']:
128             return self.val*100000
129         elif self.unit in ['kpa', 'kPa', 'KPA']:
130             return self.val*1000
131         elif self.unit in ['pa', 'Pa', 'PA']:
132             return self.val*1
133         elif self.unit in ['atm', 'ATM', 'atmospheres']:
134             return self.val*101325
135         elif self.unit in ['torr', 'Torr', 'TORR', 'mmHg', 'MMHG']:
136             return self.val*133.322368
137         elif self.unit in ['inH2O', 'inh2o', 'INH2O', 'inchH2O']:
138             return self.val*249.17400
139         else:
140             print('Error when trying to convert something to Pa')
141     def to_torr(self):
142         if self.unit in ['psi', 'PSI']:
143             return self.val*51.7149326
144         elif self.unit in ['mpa', 'MPa', 'MPA']:
145             return self.val*7500.61683
146         elif self.unit in ['bar', 'Bar', 'BAR']:
147             return self.val*750.061683
148         elif self.unit in ['kpa', 'kPa', 'KPA']:
149             return self.val*7.50061683
150         elif self.unit in ['pa', 'Pa', 'PA']:
151             return self.val*0.0750061683
152         elif self.unit in ['atm', 'ATM', 'atmospheres']:
153             return self.val*760
154         elif self.unit in ['torr', 'Torr', 'TORR', 'mmHg', 'MMHG']:
155             return self.val*1
156         elif self.unit in ['inH2O', 'inh2o', 'INH2O', 'inchH2O']:
157             return self.val*1.8689587
```

```
158             else:
159                 print('Error when trying to convert something to torr')
160         def to_mmHg(self):
161             if self.unit in ['psi', 'PSI']:
162                 return self.val*51.7149326
163             elif self.unit in ['mpa', 'MPa', 'MPA']:
164                 return self.val*7500.61683
165             elif self.unit in ['bar', 'Bar', 'BAR']:
166                 return self.val*750.061683
167             elif self.unit in ['kpa', 'kPa', 'KPA']:
168                 return self.val*7.50061683
169             elif self.unit in ['pa', 'Pa', 'PA']:
170                 return self.val*0.0750061683
171             elif self.unit in ['atm', 'ATM', 'atmospheres']:
172                 return self.val*760
173             elif self.unit in ['torr', 'Torr', 'TORR', 'mmHg', 'MMHG']:
174                 return self.val*1
175             elif self.unit in ['inH2O', 'inh2o', 'INH2O', 'inchH2O']:
176                 return self.val*1.8689587
177             else:
178                 print('Error when trying to convert something to mmHg')
179         def to_atm(self):
180             if self.unit in ['psi', 'PSI']:
181                 return self.val*0.0680459639
182             elif self.unit in ['mpa', 'MPa', 'MPA']:
183                 return self.val*9.86923267
184             elif self.unit in ['bar', 'Bar', 'BAR']:
185                 return self.val*0.986923267
186             elif self.unit in ['kpa', 'kPa', 'KPA']:
187                 return self.val*0.00986923267
188             elif self.unit in ['pa', 'Pa', 'PA']:
189                 return self.val*0.00000986923267
190             elif self.unit in ['atm', 'ATM', 'atmospheres']:
191                 return self.val*1
192             elif self.unit in ['torr', 'Torr', 'TORR', 'mmHg', 'MMHG']:
```

```
193             return self.val*0.00131578947
194         elif self.unit in ['inH2O', 'inh2o', 'INH2O', 'inchH2O']:
195             return self.val*0.00245915618
196         else:
197             print('Error when trying to convert something to atm')
198     def to_inH2O(self):
199         if self.unit in ['psi', 'PSI']:
200             return self.val*27.6704523
201         elif self.unit in ['mpa', 'MPa', 'MPA']:
202             return self.val*4013.25981
203         elif self.unit in ['bar', 'Bar', 'BAR']:
204             return self.val*401.325981
205         elif self.unit in ['kpa', 'kPa', 'KPA']:
206             return self.val*4.01325981
207         elif self.unit in ['pa', 'Pa', 'PA']:
208             return self.val*0.00401325981
209         elif self.unit in ['atm', 'ATM', 'atmospheres']:
210             return self.val*406.64355
211         elif self.unit in ['torr', 'Torr', 'TORR', 'mmHg', 'MMHG']:
212             return self.val*0.535057303
213         elif self.unit in ['inH2O', 'inh2o', 'INH2O', 'inchH2O']:
214             return self.val*1
215         else:
216             print('Error when trying to convert something to inches of H2O')
```

Algorithm B.4: Importing data

```
1 # String of LabVIEW data acquisition file for the test loop in 'filename'
2 LV_data = pd.read_csv('filename', sep='\t')
3 numData = len(LV_data['time [s]'][:])
4 endTime = LV_data['time [s]'][numData-1]
5 print('Number of Data Points:        ' + str(numData))
6 print('Total Runtime:                ' + str(endTime) + ' [s]')
7
8 # start = 0; end = numData-1
9 print('Start/End interval duration: ' + str(LV_data['time [s]'][end] -\
```

```
10        LV_data['time [s]'][start]) + '[s]')
```

Algorithm B.5: Heat input and mass-flow through global measures

```
1  i    = 0
2  avg = 4
3  times = []
4  h_in = []
5  h_out = []
6  dens_in  = []
7  dens_out = []
8  phases_in = []
9  phases_out = []
10
11 while i + avg + start < end:
12     ''' Find local P and T at TS in/outlet as average '''
13     locPin  = np.mean(LV_data['testsec_in_psi'][start+i:start+i+avg])
14     locPout = np.mean(LV_data['testsec_out_psi'][start+i:start+i+avg])
15     locTin  = np.mean(LV_data['testsec_in_C'][start+i:start+i+avg])
16     locTout = np.mean(LV_data['testsec_out_C'][start+i:start+i+avg])
17     locTime = np.mean(LV_data['time [s]'][start+i:start+i+avg])
18
19     ''' Determine h and d at in/outlet and the phases '''
20     locH_in   = CPCP.PropsSI('H', 'T', locTin+273.15, 'P', psi2(locPin, 'Pa'), fluid)
21     locH_out  = CPCP.PropsSI('H', 'T', locTout+273.15, 'P', psi2(locPout, 'Pa'), fluid)
22     locD_in   = CPCP.PropsSI('D', 'T', locTin+273.15, 'P', psi2(locPin, 'Pa'), fluid)
23     locD_out  = CPCP.PropsSI('D', 'T', locTout+273.15, 'P', psi2(locPout, 'Pa'), fluid)
24     phase_in  = CPCP.PhaseSI('T', locTin+273.15, 'P', psi2(locPin, 'Pa'), fluid)
25     phase_out = CPCP.PhaseSI('T', locTout+273.15, 'P', psi2(locPout, 'Pa'), fluid)
26
27     phases_in.append(phase_in)
28     phases_out.append(phase_out)
29
30     ''' Save desired parameters in arrays '''
31     times.append(locTime)
32     dens_in.append(locD_in)
```

```
33      dens_out.append(locD_out)
34      h_in.append(locH_in)
35      h_out.append(locH_out)
36
37      i += avg
38
39  dens_avg = (np.array(dens_in) + np.array(dens_out))/2
40  deltaH   = ((np.array(h_out) - np.array(h_in))*dens_avg)*(chan_h*chan_L*chan_w)
41
42  avgCPin = CPCP.PropsSI('CPMASS', 'T', np.mean(LV_data['testsec_in_C'][start:end])+273.15, \
43          'P', psi2(np.mean(LV_data['testsec_in_psi'][start:end]), 'Pa'), fluid)
44  avgCPout = CPCP.PropsSI('CPMASS', 'T', np.mean(LV_data['testsec_out_C'][start:end])+273.15,
45          'P', psi2(np.mean(LV_data['testsec_out_psi'][start:end]), 'Pa'), fluid)
46  meanTempIn  = np.mean(LV_data['testsec_in_C'][start:end])
47  meanTempOut = np.mean(LV_data['testsec_out_C'][start:end])
48  avgTempChange = meanTempOut -  meanTempIn
49  avgFlowrate = sum(LV_data['flowrate_mL/s'][start:end])/(end-start)
50  massFlow = avgFlowrate * np.mean(dens_avg)/1e6
51  heatRate_est = massFlow * np.mean(avgCPin+avgCPout) * avgTempChange
```

Algorithm B.6: Heat input and mass-flow through fin flux measrues

```
1  meanTempIn  = np.mean(LV_data['testsec_in_C'][start:end])
2  meanTempOut = np.mean(LV_data['testsec_out_C'][start:end])
3  meanPresIn  = np.mean(LV_data['testsec_in_psi'][start:end])
4  meanPresOut = np.mean(LV_data['testsec_out_psi'][start:end])
5  meanPres    = (meanPresIn + meanPresOut)/2
6  diffInOut   = meanTempOut - meanTempIn
7  tempsTop = []; tempsBottom = []
8  tempsTop.append(meanTempIn); tempsBottom.append(meanTempIn)
9
10 count = 1
11 while count < 13:
12   top    = 'TC' + str(count) + 't'
13   bottom = 'TC' + str(count) + 'b'
14   locTopTemp = np.mean(LV_data[top][start:end])
```

```
15      locBotTemp = np.mean(LV_data[bottom][start:end])
16      tempsTop.append(locTopTemp)
17      tempsBottom.append(locBotTemp)
18      count += 1
19
20  tempsTop.append(meanTempOut)
21  tempsBottom.append(meanTempOut)
22
23  topTempArray = np.array(tempsTop)
24  botTempArray = np.array(tempsBottom)
25
26  qDot_TS = Al_k * fin_w * fin_th * (botTempArray - topTempArray)/0.01
27
28  dAs = 2*(chan_h + chan_w)*chan_L/20
29
30  heatTemp  = [tempsBottom[1], np.mean(tempsBottom[1:3]), tempsBottom[2],
31      np.mean(tempsBottom[2:4]), tempsBottom[3], np.mean(tempsBottom[3:5]), tempsBottom[4],
32      np.mean(tempsBottom[4:6]), tempsBottom[5], tempsBottom[6], tempsBottom[7],
33      tempsBottom[8], np.mean(tempsBottom[8:10]), tempsBottom[9], np.mean(tempsBottom[9:11]),
34      tempsBottom[10], np.mean(tempsBottom[10:12]), tempsBottom[11],
35      np.mean(tempsBottom[11:13]), tempsBottom[12]]
36
37  wallTemp  = [tempsTop[1], np.mean(tempsTop[1:3]), tempsTop[2], np.mean(tempsTop[2:4]),
38      tempsTop[3], np.mean(tempsTop[3:5]), tempsTop[4], np.mean(tempsTop[4:6]),
39      tempsTop[5], tempsTop[6], tempsTop[7], tempsTop[8], np.mean(tempsTop[8:10]),
40      tempsTop[9], np.mean(tempsTop[9:11]), tempsTop[10], np.mean(tempsTop[10:12]),
41      tempsTop[11], np.mean(tempsTop[11:13]), tempsTop[12]]
42
43  heatArray = [qDot_TS[1], np.mean(qDot_TS[1:3]), qDot_TS[2], np.mean(qDot_TS[2:4]),
44      qDot_TS[3], np.mean(qDot_TS[3:5]), qDot_TS[4], np.mean(qDot_TS[4:6]),
45      qDot_TS[5], qDot_TS[6], qDot_TS[7], qDot_TS[8], np.mean(qDot_TS[8:10]),
46      qDot_TS[9], np.mean(qDot_TS[9:11]), qDot_TS[10], np.mean(qDot_TS[10:12]),
47      qDot_TS[11], np.mean(qDot_TS[11:13]), qDot_TS[12]]
48
49  heatInputErr = max(abs(sum(heatArray)*2 - heatRate_est)/(sum(heatArray)*2)*100,
```

```
50                      abs(sum(heatArray)*2 - heatRate_est)/heatRate_est*100)
51
52 fldSat_T = CPCP.PropsSI('T', 'P', psi2(meanPres, 'Pa'), 'Q', 1., fluid)-273.15
53 liqSat_H = CPCP.PropsSI('H', 'P', psi2(meanPres, 'Pa'), 'Q', 0., fluid)
54 vapSat_H = CPCP.PropsSI('H', 'P', psi2(meanPres, 'Pa'), 'Q', 1., fluid)
55 heatVap  = vapSat_H - liqSat_H
56 vapWatts = heatVap*massFlow
```

Algorithm B.7: Calculation of local fluid temps, convective coefficient, and Nu number

```
1  n = 0
2  fldTemp = []
3  fldTemp.append(meanTempIn)
4  while n < 20:
5      locCP = CPCP.PropsSI('CPMASS', 'T', fldTemp[n]+273.15, 'P', psi2(meanPres, 'Pa'),
6                           'R134a')
7      dT    = (2*heatArray[n] / ((massFlow) * locCP))
8      newT  = fldTemp[n] + dT
9      if fldTemp[n]<fldSat_T and newT>fldSat_T:
10         jPERkg = locCP*(newT-fldSat_T)
11         while jPERkg < heatVap and n < 20:
12             # print(jPERkg/heatVap)
13             jPERkg += 2*heatArray[n]/massFlow
14             if jPERkg > heatVap:
15                 dT = (jPERkg - heatVap)/locCP
16                 newT = fldSat_T + dT
17             else:
18                 fldTemp.append(fldSat_T)
19                 n +=1
20     fldTemp.append(newT)
21     n += 1
22 fldTemp.append(meanTempOut)
23
24 j = 0
25 hArray  = []
26 NuArray = []
```

```
27 while j < 20:
28     fldTemp_avg = np.mean(fldTemp[j:j+2])
29     h = heatArray[j]/(dAs * (wallTemp_res[j] - fldTemp_avg))
30     hArray.append(h)
31     pLoc = meanPresIn + (meanPresOut - meanPresIn)/20*(j+1)
32     kLoc = CPCP.PropsSI('L', 'P', pi2(pLoc, 'Pa'), 'T', fldTemp_avg+273.15, 'R134a')
33     NuLoc = (h*(chan_L/20))/kLoc
34     NuArray.append(NuLoc)
35     j+=1
```

B.2 LabVIEW Diagram

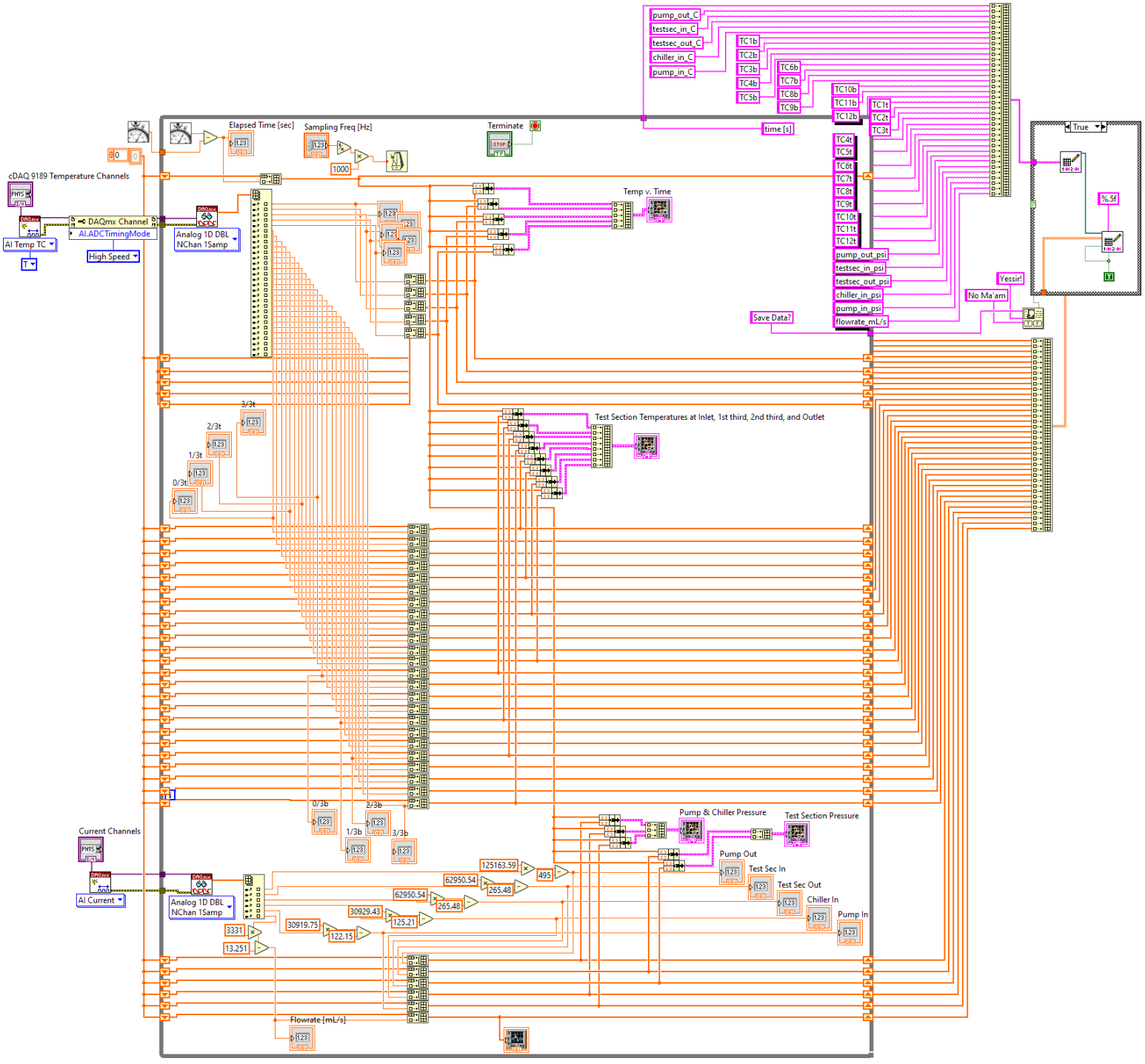

Fig. B.1: Block diagram of the data acquisition program